

Air Force Institute of Technology

AFIT Scholar

[Theses and Dissertations](#)

[Student Graduate Works](#)

3-2005

Daytime Detection of Space Objects

Alistair D. Funge

Follow this and additional works at: <https://scholar.afit.edu/etd>

 Part of the [Engineering Physics Commons](#), and the [Signal Processing Commons](#)

Recommended Citation

Funge, Alistair D., "Daytime Detection of Space Objects" (2005). *Theses and Dissertations*. 3837.
<https://scholar.afit.edu/etd/3837>

This Thesis is brought to you for free and open access by the Student Graduate Works at AFIT Scholar. It has been accepted for inclusion in Theses and Dissertations by an authorized administrator of AFIT Scholar. For more information, please contact richard.mansfield@afit.edu.



DAYTIME DETECTION OF SPACE OBJECTS

THESIS

ALISTAIR D. FUNGE, CAPTAIN, USAF

AFIT/GAP/ENG/05-01

**DEPARTMENT OF THE AIR FORCE
AIR UNIVERSITY**

AIR FORCE INSTITUTE OF TECHNOLOGY

Wright-Patterson Air Force Base, Ohio

APPROVED FOR PUBLIC RELEASE; DISTRIBUTION UNLIMITED

The views expressed in this thesis are those of the author and do not reflect the official policy or position of the United States Air Force, Department of Defense, or the U.S. Government.

AFIT/GAP/ENG/05-01

DAYTIME DETECTION OF SPACE OBJECTS

THESIS

Presented to the Faculty

Department of Electrical and Computer Engineering

Graduate School of Engineering and Management

Air Force Institute of Technology

Air University

Air Education and Training Command

In Partial Fulfillment of the Requirements for the

Degree of Master of Science in Applied Physics

Alistair D. Funge, BS, ME

Captain, USAF

March, 2005


APPROVED FOR PUBLIC RELEASE; DISTRIBUTION UNLIMITED

DAYTIME DETECTION OF SPACE OBJECTS

Alistair D. Funge, BS, ME


Captain, USAF

Approved:




Maj Matthew E. Goda, USAF (Chairman)

9 MAR 05
Date



Dr. Michael A. Marciniak (Member)

8 MAR 05
Date



Dr. Richard G. Cobb (Member)

9 MAR 05
Date

Abstract

Space Situational Awareness (SSA) requires repeated object updates for orbit accuracy. Detection of unknown objects is critical. A daytime model was developed that evaluated sun flares and assessed thermal emissions from space objects.

Iridium satellites generate predictable sun glints. These were used as a model baseline for daytime detections. Flares and space object thermal emissions were examined for daytime detection. A variety of geometric, material and atmospheric characteristics affected this daytime detection capability.

In a photon noise limited mode, simulated Iridium flares were detected. The peak Signal-to-Noise Ratios (SNR) were $6.05e18$, $9.63e5$, and $1.65e7$ for the nighttime, daytime and infrared flares respectively.

The thermal emission of space objects at 353K, 900K and 1300K with 2 to 20 m² emitting areas were evaluated. The peak emission was for the 20 m² 900K object with an SNR of $1.08e10$.

A number of barriers remain to be overcome if daytime detection of space objects can be achieved. While the above SNR values are large, this is based on optimal detection. The SBR's were less than 1 for all cases. Image post-processing will be necessary to extract the object from the background.

Successful daytime detection techniques will increase sensor utilization times and improve SSA.

Acknowledgments

I would like to express my sincere appreciation to my faculty advisor, Maj Matt Goda, for his guidance and support throughout the course of this thesis effort. The efforts of the committee members, Dr. Michael Marciniak and Dr. Richard Cobb in keeping me on the straight and narrow, are greatly appreciated. Much thanks also to Capt Ruben Martinez, whose Matlab[®] model I borrowed gingerly from. Thanks to the Engineering-Physics Department and Dr. Bailey for keeping on course, despite my tens years of absence from the physics world. Finally, I must thank my wonderful family and loving wife, for whom I am eternally grateful.

Alistair D. Funge

Table of Contents

	Page
Abstract.....	v
Acknowledgments.....	vi
Table of Contents.....	vii
List of Figures.....	xi
List of Tables.....	xiii
I. Introduction.....	1
1.1 Background.....	1
1.2 Problem Statement.....	2
1.3 Relevance and Expected Results.....	3
1.4 Research Objectives and Issues.....	4
1.5 Research Approach.....	4
1.6 Assumptions/Limitations.....	5
1.7 Implications.....	7
1.8 Preview.....	7
II. Background Theory.....	8
2.1 Chapter Overview.....	8
2.2 Basic Definitions.....	8
2.2.1 Steradian.....	8
2.2.2 Coordinated Universal Time (UTC).....	8
2.2.3 Spectral Radiance.....	9
2.2.4 Emissivity.....	10
2.2.5 Diffraction Limit.....	10

2.2.6	Specular Reflections.....	11
2.2.7	Signal-to-Noise Ratio.....	12
2.3	Satellite Reflections.....	13
2.3.1	Bi-directional Reflection Distribution Functions.....	14
2.3.2	Spectral Reflectance.....	18
2.4	Atmospheric Attenuation.....	19
2.5	Iridium Satellite Constellation.....	23
2.6	Satellite Flares.....	25
2.6.1	Iridium Flares.....	26
2.7	Magnitudes and Flux.....	27
2.8	Satellite model.....	27
2.9	Thermal Emissions.....	28
2.10	Summary.....	30
III.	Methodology.....	31
3.1	Chapter Overview.....	31
3.2	Satellite in Field-of-View.....	31
3.3	Orbit Determination.....	31
3.4	Satellite Attitude Determination.....	31
3.5	Satellite Geometries.....	33
3.5.1	Sun-Satellite and Satellite-Sensor Geometry.....	34
3.5.2	Satellite Tool Kit.....	34
3.5.3	Units.....	35
3.6	Numerical Process.....	36

3.6.1 Panel Projected Area	36
3.6.2 Spectral Reflectance	37
3.6.3 Silvered Teflon and Aluminized BRDF's	39
3.6.4 Atmospheric Attenuation.....	40
3.7 Thermal Emissions	40
3.8 Signal-to-Noise Ratios.....	41
3.9 Problems Encountered.....	41
3.10 Summary.....	42
IV. Analysis and Results.....	43
4.1 Chapter Overview.....	43
4.2 Iridium Flare Results	43
4.2.1 Iridium 40 Nighttime Flare.....	44
4.2.2 Iridium 72 Daytime Flare	50
4.2.3 Simulated 'Flare' Results	53
4.2.4 Infrared Flares	55
4.2.5 Visible Versus Infrared Flares.....	57
4.3 Thermal Emissions	59
4.4 Summary.....	60
V. Conclusions and Recommendations	62
5.1 Chapter Overview.....	62
5.2 Conclusions of Research	62
5.3 Significance of Research	63
5.4 Recommendations for Future Research.....	63

5.5 Summary.....	65
VI. Appendix.....	66
1. Matlab® Iridium Satellite Model Source Code.....	66
2. Iridium Two Line Element (TLE) Set	80
Bibliography	89
Vita	92

List of Figures

	Page
Figure 1. Photon Reflection Process.....	5
Figure 2. Sun's blackbody curve at 5777 K before atmospheric attenuation.....	10
Figure 3. Specular vs. diffuse reflections	11
Figure 4. BRDF reflection geometry	15
Figure 5. BRDF output response for a light ray with fixed input direction.....	16
Figure 6. Sample BRDF for aluminized mylar	17
Figure 7. Photograph showing near specular reflection from an MMA.....	18
Figure 8. Spectral reflectance for aluminized kapton	19
Figure 9. Visible and infrared atmospheric attenuation profile from PLEXUS	21
Figure 10. PLEXUS output display interface	22
Figure 11. Iridium orbital planes	24
Figure 12. Artist concept of Iridium satellite	24
Figure 13. One minute exposure of Iridium 12 flare	25
Figure 14. Iridium satellite model generated using Matlab [®] code in appendix 1.....	28
Figure 15. Reflectance of aluminized kapton and mylar	38
Figure 16. Solar radiance reflected off of satellite main mission antennas	38
Figure 17. Normalized BRDF's from Optical Measurement Facility data.....	39
Figure 18. Iridium 40 flare.....	46
Figure 19. Iridium 40 flare irradiance due to pointing errors	47
Figure 20. Magnitude of nighttime flare vs. predictions	48

Figure 21. Effect of attitude errors on nighttime flare magnitude	49
Figure 22. Nighttime flare SNR.....	49
Figure 23. Iridium 72 flare with 0.01 degree field-of-view.....	51
Figure 24. Magnitude of daytime flare vs. predictions.....	51
Figure 25. Daytime flare Signal-to-Noise Ratio (0.01 deg FOV).....	53
Figure 26. SNR for miscellaneous flares geometries.....	54
Figure 27. SNR for broadband infrared flare.....	56
Figure 28. SNR for narrowband infrared flare.....	56
Figure 29. Comparison of narrowband and broadband infrared flares.....	57
Figure 30. Visible and near IR atmospheric transmittance spectrum from PLEXUS	58
Figure 31. Comparison of SNR's for visible and infrared flares.....	59
Figure 32. Signal-to-Noise Ratios for various space objects.....	60

List of Tables

	Page
Table 1. Thermal Emission Characteristics	30
Table 2. IRIDFLAR predictions for Maui	43
Table 3. Iridium 40 nighttime flare irradiance.....	44
Table 4. Iridium 40 Nighttime Flare Magnitudes	45
Table 5. Iridium 72 Daytime Flare Irradiance	50
Table 6. Background Irradiance as a function of slant range and flare angle.....	52
Table 7. Space object thermal characteristics	59

DAYTIME DETECTION OF SPACE OBJECTS

I. Introduction

1.1 Background

“If the U.S. is to avoid a Space Pearl Harbor, it needs to take seriously the possibility of an attack on U.S. space systems.”¹

In January, 2001, the Space Commission released its report evaluating how U.S. space assets are used in support of U.S. national security. One of the key findings of the Commission was that it is in the U.S. national interest to develop and deploy the means to deter and defend against hostile acts directed at U.S. space assets and against the uses of space by hostile parties against U.S. interests. Pursuant to this finding, the Commission recommended departments and agencies of the U.S. Government develop revolutionary methods of collecting intelligence from space. As an outcome of the Commission’s report, the Secretary of Defense designated the Air Force as Executive Agent for Space within the Department of Defense.

The United States Air Force mission statement is to, “Defend the United States through control and exploitation of air and space.”² Control and exploitation of space requires knowledge of what is in orbit around the Earth.

The Space Control mission area ensures the freedom of operations within and throughout the space medium, while denying its use to adversaries. Space Control includes three sub-missions: Space Situational Awareness (SSA), Defensive Counterspace and Offensive Counterspace.

SSA is the foundation of Space Control and includes activities to provide predictive surveillance of all resident space objects. SSA helps to ensure the safe flight of satellites and launch platforms, determine when space operations are necessary and possible, evaluate impacts from the space environment on operations, identify, characterize and monitor all potential threats to friendly space assets and adversary space capabilities which pose a threat to friendly terrestrial forces, and make after-action assessments.³ The optical sensors of the Space Surveillance Network (SSN) are critical in maintaining accurate SSA.

1.2 Problem Statement

Satellites in Low Earth Orbit (LEO) present several detection and tracking problems for ground-based optical sensors. Three lighting conditions exist that affect the ability of space objects to be detected. The best situation is when the ground sensor is in the Earth's shadow, while the satellite is sunlit. The next is when the satellite and sensor are both in the Earth's shadow. The final occurrence is when the sensor and satellite are sunlit. It is extremely difficult to detect most space objects during the day. Successful methods to detect LEO satellites during the day will greatly improve sensor utilization times of the SSN and our SSA overall.

In order to develop these daytime detection tools, we must first develop methods for detecting satellites in somewhat controlled conditions and for expanding our toolset as our understanding improves. An interesting case study is that of sun glints or flares off of Iridium communication satellites.

Shortly after their initial launch, amateur satellite observers reported seeing flares,

or a sudden, but temporary, flash of light coming from the passing Iridium satellites. It did not take long for knowledgeable spacecraft engineers to speculate that the flashes of light may be due to sunlight reflecting off of the Main Mission Antennas (MMA) on the satellite. The satellite geometry and attitude was confirmed by engineers working for the spacecraft operator. Shortly afterwards, flare prediction tools began to appear.

Iridium flares are typically observed in the visible spectrum. However, they are also observable in the infrared spectrum. The sun's blackbody curve peaks in the visible and falls off rapidly with increasing wavelength. Solar reflections from space objects typically dominate thermal emissions for objects cooler than about 500 K. This needs to be looked at to evaluate daytime detectability.

1.3 Relevance and Expected Results

Modeling a known satellite in the night sky is the first step in moving towards a daytime detection model. The differences are primarily due to the large increase in background sky radiance during the day. There is also the great difficulty in modeling space objects with unknown geometries and positions. It is expected that the techniques utilized in this thesis can accurately model the predicted flares during the night and day.

This thesis will also evaluate space object detection in the infrared portion of the spectrum. Infrared Iridium flares will be evaluated to determine if this is a more useful enterprise. Thermal emissions are a function of a body's temperature. Given the continuous emissions from satellites, this is a more frequent occurrence than satellite flares.

1.4 Research Objectives and Issues

The first objective of this thesis was to develop an Iridium satellite model to be used to determine the radiance of the Iridium flares. This will be done for several different orbital positions and sensor-satellite-sun geometries. The model will then be used to determine the flare and path radiance before, during, and after the flare event. The second objective was to evaluate the detectability of thermal emissions from space objects during the daytime.

Issues to resolve included: What surfaces on the Iridium satellite are capable of producing flares? What are the favorable sensor-satellite-sun geometries that produce flares? How much of the reflected sunlight was attenuated by the atmosphere? What was the radiance before and after the flare? For thermal emissions, what was the temperature of observed satellites? What materials and emissivities can we expect to find on space objects? What are the sizes of the emitting hot spots on these objects?

1.5 Research Approach

There were several steps in producing this thesis. These included, building a computer model of the satellite to determine projected areas with respect to the sun and the ground sensor. Bi-directional Reflectance Distribution Functions (BRDF's) were used to measure the amount of reflected light and direction of the reflection from the satellite. Atmospheric attenuation must also be accounted for. Multiple simulations were run for comparison of different sensor-satellite-sun geometries. The received irradiance was compared to the background irradiance to determine if the object is detectable. Various sensor fields-of-view were analyzed in this respect. Figure 1 diagrams the

general description of how the general process of measuring reflected sunlight from a satellite worked.

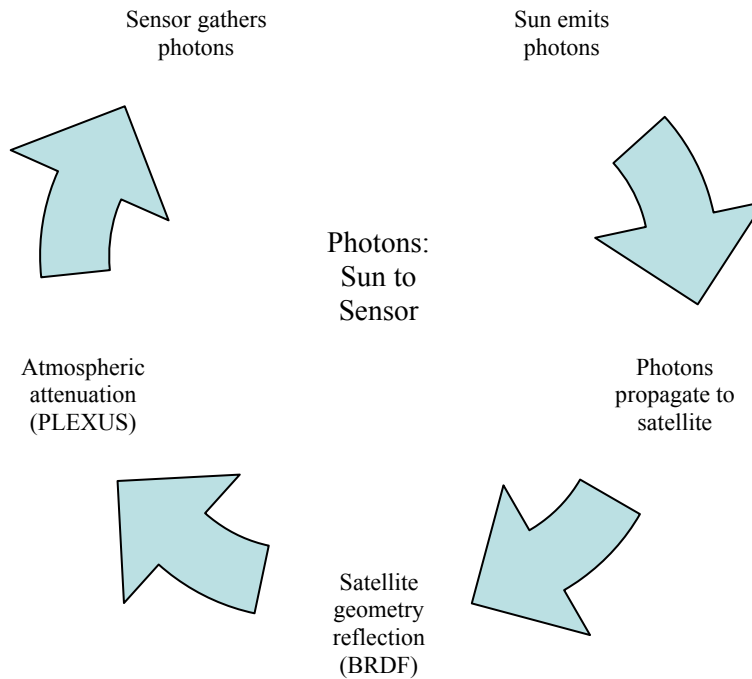


Figure 1. Photon Reflection Process

1.6 Assumptions/Limitations

Several assumptions have been made in order to simplify the flare modeling. The first was that the satellite attitude was well known. This was a reasonable assumption as the Iridium satellite was designed to rotate once per orbit while maintaining one of the MMA's orientated in the direction of motion. However, due to the distances involved, even a small attitude error can result in significant differences in the predicted flare irradiance.

Another assumption was that the solar panels would not contribute to the flares.

This was made because the panels are sun tracking. They would be orientated to near normal relative to the satellite-sun direction. Flares could be produced by the solar panels only if the sun-Satellite-Sensor geometry were such that the sun and the satellite were in near opposition with respect to the ground sensor. This geometric configuration was not tested.

A third assumption was that the atmospheric conditions would be near optimum. This was relatively reasonable, as optical sensors are usually located high on top of mountains or isolated in a dry desert where the weather is predictable and the 'seeing' is stable. Real-world atmospheric conditions could, however, degrade the capabilities of an optical sensor. Empirical studies would need to account for the less pristine seeing conditions, as required.

For thermal emissions, it was assumed that the radiating panel had relatively high emissivity. The radiators were chosen to match typical satellite radiators for size and emissivity.

Limitations of the flare model include the relative simplicity of the satellite computer model. The model does not include some smaller surfaces contributing to the flares. It also assumes that the reflecting surfaces are relatively smooth and have experienced no significant degradation due to the space environment.

Other limitations include the non-availability of reflectance data for the specific material coating the main reflecting surface on the Iridium satellite. Two close approximations were used.

This computer reflection model was purposely built for Iridium satellites. These

satellites have a very specific and well known geometry. They also have a relatively predictable attitude. These factors, however, allow models to be built to accurately confirm the flare prediction tools. This can then be expanded to model more complex geometries and space objects in unknown orbits. Ultimately, this will lead to a tool that can be used to determine the sensor requirements used to detect space objects during the daytime.

1.7 Implications

Frequent space catalog updates are critical to maintaining SSA. Attempts by hostile space forces to maneuver close to U.S. or allied on-orbit assets need to be dealt with in a timely manner. Having a better understanding of how satellites can be tracked and detected may eventually lead to daytime detection. Increasing the utilization of ground based optical telescopes through the use of daytime detection will improve our SSA.

1.8 Preview

Chapter II will review the definitions, techniques and existing models used in the analysis of this thesis. Chapter III explores the methodology for the simulations in this model. It discusses each step in the process in detail. Chapter IV discusses the results of the flare experiments and thermal emissions. Chapter V draws some conclusions about this study and makes some recommendations for the future. Chapter V also includes recommendations for improvements on the model, and how to move forward towards daytime detection.

II. Background Theory

2.1 Chapter Overview

The purpose of this chapter is to describe the existing research in this area and discuss some of the concepts used for this model.

2.2 Basic Definitions

2.2.1 Steradian

A steradian is defined as the solid (spatial) angle which, having its vertex at the center of the sphere, projects to an area equal to the square of its radius. So, 1 steradian has a projected area of 1 square meter at a distance of 1 meter. A sphere consists of 4π steradians.

2.2.2 Coordinated Universal Time (UTC)

The times of various events, particularly astronomical and weather phenomena, are often given in "Universal Time" (UT) which was sometimes referred to as "Greenwich Mean Time" (GMT). The two terms are often used loosely to refer to time kept on the Greenwich meridian (longitude zero), five hours ahead of Eastern Standard Time.

In the most common civil usage, UT refers to a time scale called "Coordinated Universal Time" (UTC), which was the basis for the worldwide system of civil time. This time scale was kept by time laboratories around the world, including the U.S. Naval Observatory, and was determined using highly precise atomic clocks.

2.2.3 Spectral Radiance

Planck's Radiation Law for blackbodies gives the spectral radiance of an object as a function of its temperature (T) and wavelength (λ in microns):

$$L_e(\lambda, T) = \frac{2hc^2 10^{20}}{\lambda^5 \left[\text{Exp}\left(\frac{hc 10^6}{\lambda k T}\right) - 1 \right]} \quad \left[\frac{\text{watts}}{\text{cm}^2 \mu \text{Sr}} \right] \quad (1)$$

where h is Planck's constant, c is the speed of light and k is Boltzmann's constant.⁴

The plot of the radiance from the sun ($T = 5777 \text{ K}$) is shown in Figure 2. The peak of the curve was determined using Wien's Displacement Law:⁵

$$\lambda_{peak}(T) = \frac{2897.8}{T} [\mu] \quad (2)$$

As can be seen from the plot, the peak lies at approximately 0.5 microns. The visible region of the curve, between 0.4 microns and 0.7 microns accounts, for less than half the total radiant output of the sun.

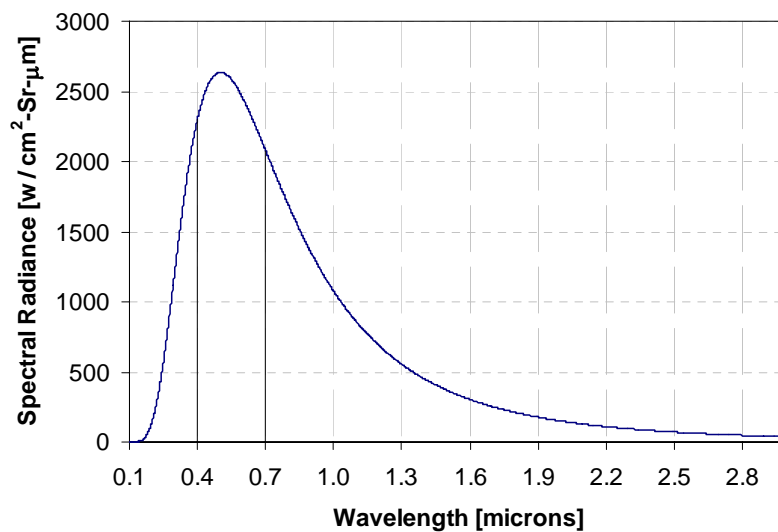


Figure 2. Sun's blackbody curve at 5777 K before atmospheric attenuation

2.2.4 Emissivity

All substances emit radiation with an exitance across all wavelengths proportional to the fourth power of temperature according to the Stefan-Boltzmann Law, $M_e(T) = \sigma_e T^4$, where σ_e is the Stefan-Boltzmann constant.⁶ This represents the maximum radiant exitance of an object at each wavelength for any given temperature. The energy emitted from these objects is normally referred to as blackbody radiation. Most substances, however, are gray bodies, in that they fail to reach this theoretical maximum radiative exitance. In order to compare the actual to theoretical emission, a concept called emissivity was defined. It was simply the ratio of the actual emitted radiance to that of an ideal blackbody at the same temperature.

The radiation temperature, T_R , can be calculated from the true temperature, T , of a gray body through the following relation:

$$T_R = \varepsilon^{\frac{1}{4}} T \quad [\text{K}] \quad (3)$$

where ε is the emissivity of the substance.⁷ The radiation temperature is the temperature of the blackbody that would give the same area under the spectral exitance curve across all wavelengths as the source being measured.

2.2.5 Diffraction Limit

The diffraction limit is the physical resolution limit due to the diffraction of light in optical devices. This minimum angular resolution was defined by:

$$\theta_{\min} = \frac{1.22\lambda}{D} \quad [\text{rad}] \quad (4)$$

where D is the diameter of the optics or telescope.⁸

Atmospheric turbulence limits the observed angular resolution to approximately 0.25 to 3.0 arc-second - this is known as 'seeing', and the seeing describes the limits the atmosphere places on angular resolution. However, the diffraction limit of large telescopes can be a factor of 10-50 times better than this, depending on the observing wavelength and the diameter of the telescope. With instrumentation which rapidly samples the instantaneous 'speckle pattern', near diffraction-limited imaging can sometimes be achieved.⁹

2.2.6 Specular Reflections

Reflection off of smooth surfaces such as mirrors or a calm body of water leads to a type of reflection known as specular reflection. Reflection off of rough surfaces such as clothing, paper, and the asphalt roadway leads to a type of reflection known as diffuse reflection. Whether the surface is microscopically rough or smooth has a tremendous impact upon the subsequent reflection of a beam of light. Figure 3 depicts two beams of light incident upon a rough and a smooth surface.

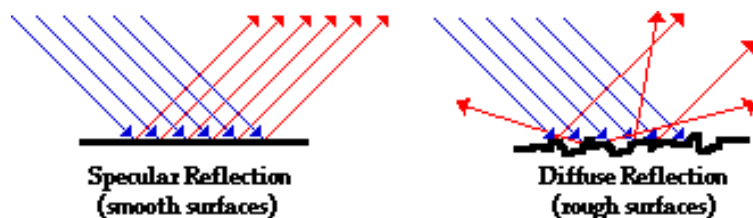


Figure 3. Specular vs. diffuse reflections¹⁰

A beam can be thought of as a bundle of individual light rays which are traveling

parallel to each other. Each individual light ray of the bundle follows the law of reflection. If the bundle of light rays is incident upon a smooth surface, then the light rays reflect and remain concentrated in a bundle upon leaving the surface. On the other hand, if the surface is microscopically rough, the light rays will reflect and diffuse in many different directions

2.2.7 Signal-to-Noise Ratio

The Signal-to-Noise Ratio (SNR) of an object is a comparison of the output signal current to that of the output noise current from a detector. In general, when the signal current is equal to or greater than the noise current ($\text{SNR} \geq 1$), we have a detectable signal.

Noise refers to any unwanted signal. There are three main types of noises sources, photon, readout and dark noise. Photon noise is a function of the signal and background. Readout noise is due to the conversion of photons to an electrical signal. Dark noise is due to the variation in thermally generated electrons in the detector. Photon-noise-limited performance is when all other noise contributions are small compared to the noise associated with the incident photon flux. This is the best possible condition. When the background photon flux is much larger than the signal flux and is the dominant noise source, we are operating in Background Limited Infrared Photodetector (BLIP) mode.

An SNR can be written

$$\frac{S}{N} = \frac{\eta E_{q,signal} A_d q}{[2q^2 \eta E_{q,background} A_d \Delta f]^{\frac{1}{2}}} \quad (5)$$

where η is the quantum efficiency (conversion efficiency of the incident photons to

output electrons on the backside of the sensor), E_q is the signal and background irradiance, A_d is the sensor area, q is the charge of an electron, and Δf is the noise-equivalent bandwidth.¹¹ An SNR of 1 determines the minimum detectable signal irradiance.

2.3 Satellite Reflections

The amount of sunlight reflected off a satellite to an observer depends on the projected areas of the satellite's reflecting surface with respect to the observer. A surface normal to the sun, or another illumination source, would reflect more light than a panel that projected a smaller area towards the light source. The amount of reflected light also depends on the material's reflectance characteristics. Materials reflect light differently, varying between specular and diffuse reflections. Prior to analyzing the material scattering it was needed to assess the angles between the reflecting surface on the satellite with respect to both the sun and the observer.

The angles measured at the satellite are those between the vector from the center of the satellite to the sun or a ground site and the vector that was normal to the reflecting panel. For the computer model of the Iridium satellite, the origins of the vectors are not both at the center of the satellite. The antenna normal vector was centered in the middle of the reflecting MMA, while the satellite-sun vector has an origin at the center of the satellite. This discrepancy of less than one meter in the origin of the two vectors was inconsequential compared to the slant ranges to the ground site (over 800 kilometers) and the range to the sun (approximately 148 million kilometers). Errors in the angles measured between the sun and the panel normal vector and the observer and the panel

normal vector are thus insignificant.

2.3.1 Bi-directional Reflection Distribution Functions

Materials can reflect, absorb or transmit incident electromagnetic waves. The vast majority of materials on the outer surface of satellites are designed to either reflect incoming sunlight or transfer energy into or out of the satellites, depending on the design and thermal needs.

Emitted energy was typically due to re-emission of energy previously absorbed or an on board power source. The peak of this energy was typically in the infrared for most satellites that operate around 300 K. However, when an observer was near a flare scattering angle, infrared emissions are typically not as large as reflected solar energy. The irradiance of flares produced by a solar reflection peaks in the visible portion of the spectrum. This reflection can come from single or multiple reflections of the sunlight.

The most common means of quantifying surface reflection of light was by utilizing the bi-directional reflectance distribution function (BRDF). The BRDF, ρ , was defined as the ratio of differential reflected radiance to differential incident irradiance:

$$\rho(\theta_i, \theta_r, \lambda) = \frac{dL_r(\theta_i, \theta_r, \lambda)}{dE_i(\theta_i, \lambda)} \quad (6)$$

where the subscripts i and r denote incident and reflected, respectively, θ and ϕ describe the direction of light propagation, λ was the wavelength of light, L was radiance, E was irradiance.¹² The surface reflection geometry is shown in Figure 4 with $d\omega$ as a solid angle.

BRDF's can be measured using either monochromatic or broadband sources.

Monochromatic sources, such as lasers, have the advantage in that the source of the light was limited to a particular direction before it strikes the material to be measured.

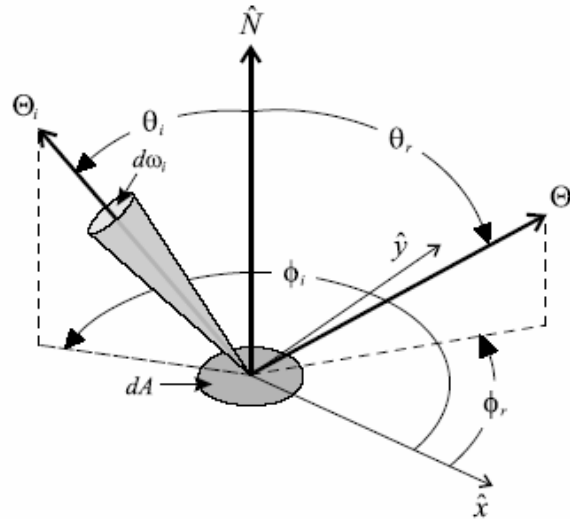


Figure 4. BRDF reflection geometry ¹³

Limiting the BRDF to an incident source from one direction, allows the measuring lab to concentrate on the material's reflectance characteristics. This also greatly simplifies the amount of measurement work necessary to produce the BRDF, albeit at the expense of some fidelity. Full geometry BRDF's are computationally complex, given that every incident angle and separate reflectance angles must be accounted for. Figure 5 was an example of what a BRDF quantifies. The lobe was the 'cone' of reflected light given incident angles, θ_i and ϕ_i .

When a beam of electromagnetic radiation (visible, infrared, radar, etc.) strikes a material interface of a body, it can scatter off the top or first surface, as well as from the volume or subsequent interfaces. The total amount of light reflected from the first surface depends primarily on the complex index of refraction of the illuminated medium

(relative to that of the incident medium) and was often sufficiently large that this dominates the scattering from the material.

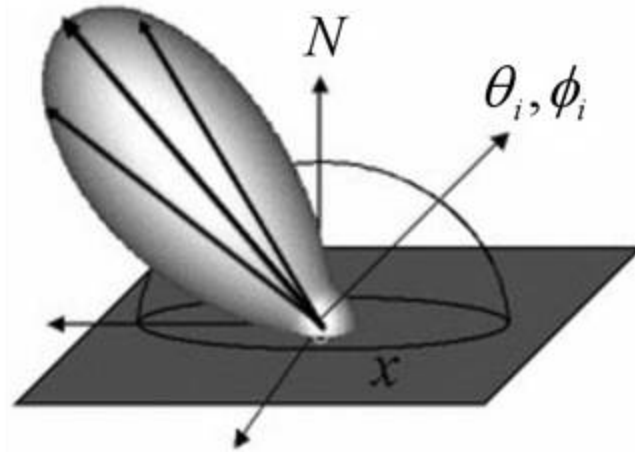


Figure 5. BRDF output response for a light ray with fixed input direction¹⁴

On the other hand, the topography of this interface determines the angular distribution of the scattered radiation—smooth surfaces reflect almost entirely into the specular direction, while with increasing roughness, the light tends to diffract into all possible directions. Ultimately, an object will appear equally bright throughout the outgoing hemisphere if its surface was perfectly diffuse (a.k.a., Lambertian). Measuring the BRDF can thus give valuable information about the nature of a target sample.

In general, theoretical models begin by considering light to be incident on a spot on the surface of an object from a range of solid angles, $d\omega_i$ (which can vary from a delta function for a fully directional beam to 2π for the hemisphere), centered on polar (zenith) angle, θ_i (defined with respect to the macroscopic surface normal), and azimuthal angle, ϕ_i (conveniently defined with respect to some sample feature in the case of an anisotropic

surface or arbitrarily for an isotropic one).

This light is transmitted, absorbed, or reflected by the object; the fraction of the incident flux, P (radiant power in W), which is subsumed by these mechanisms, is specified by the dimensionless ratios called the transmittance, τ , the absorptance, α , and the reflectance, ρ . Assuming that the illuminated object was opaque, $\tau = 0$; accordingly, $\alpha + \rho = 1$. The reflected light (which can be more generally described as scattered light) was collected by a detector spanning a solid angle, $d\omega_r$, centered on angles θ_r and ϕ_r .¹⁵

Figure 6 is a sample BRDF measured for aluminized mylar using a polarized light source generated by a helium-neon laser with an incident angle of 40 degrees.

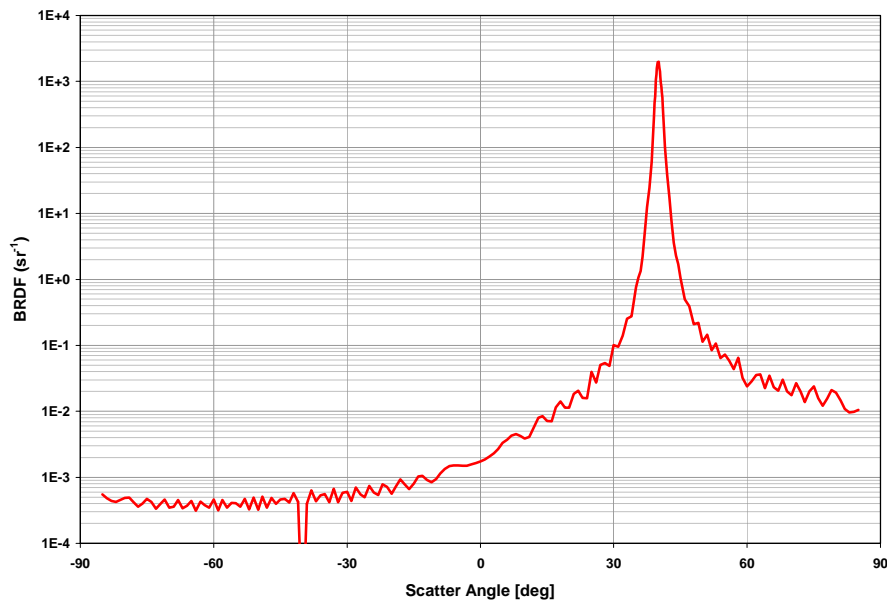


Figure 6. Sample BRDF for aluminized mylar¹⁶

This sample produced a largely specular reflection. There was some scattering occurring within a few degrees of the reflected angle, but BRDF falls off rapidly as the measurement angle moves away from the scattered angle. The Air Force Research

Laboratory (AFRL) has developed BRDF's for numerous materials.

The Main Mission Antennas are made of aluminum coated with silvered teflon. While the Air Force Research Lab's Optical Measurements Facility (OMF) had not measured such a material, they did have data on aluminized kapton and aluminized mylar. The Optical Measurements Facility estimates that aluminized kapton and aluminized mylar would have similar optical properties as silvered teflon. The OMF staff believes that the response of these materials to broad spectrum light sources was expected to be similar to the He-Ne laser data provided.¹⁷ Figure 7 shows flash photography of a Main Mission Antenna for a prototype Iridium satellite in the Smithsonian.

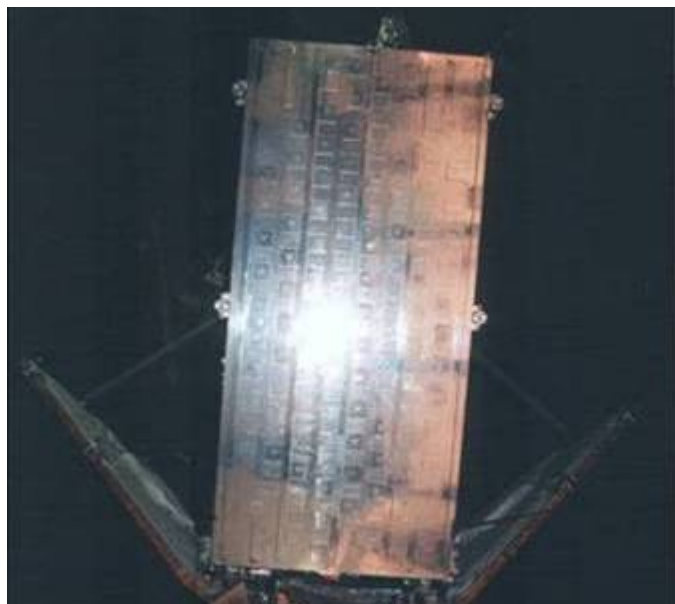


Figure 7. Photograph showing near specular reflection from an MMA¹⁸

2.3.2 Spectral Reflectance

By Snell's Law, the reflectance between two materials is dependent on the two

indices of refraction. These, in turn, vary according to wavelength or the energy passing through the material. Hence, the amount of reflected light at the interface between two different materials can vary with wavelength. This spectral reflectance behavior is shown in Figure 8.

2.4 Atmospheric Attenuation

Light passing through the Earth's atmosphere will be attenuated by one of two different mechanisms, absorption or scattering. The interaction of radiation with matter can cause either redirection of the radiation and/or transitions between the energy levels of the atoms or molecules.

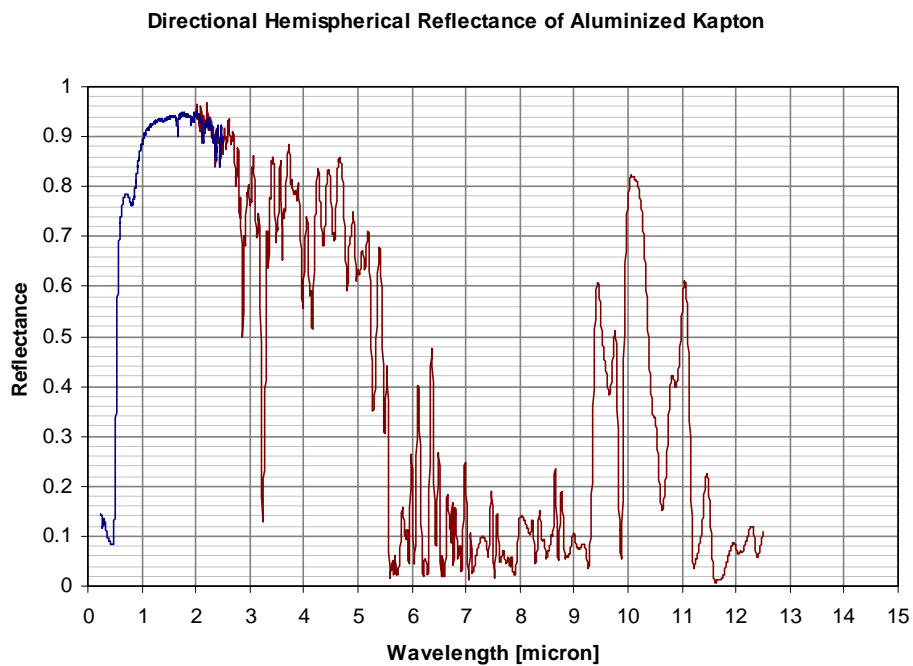


Figure 8. Spectral reflectance for aluminized kapton ¹⁹

A transition from a lower level to a higher level with transfer of energy from the

radiation to an atom or molecule is called absorption. Emission is a transition from a higher energy level to a lower level with emission of radiation. Scattering occurs when incident radiation is redirected due to its interaction with matter.

The scattering angle depends on particle size and photon wavelength. There are three types of scattering mechanisms: Rayleigh, Mie and isotropic scattering. Rayleigh scattering occurs when the particle radius is much smaller than the wavelength. Mie or aerosol scattering occurs when the wavelength is nearly the same as the particle size. Isotropic scatter occurs when the particle radius is much bigger than the wavelength of the light.

Path radiance is the production of radiation by atmospheric particles within a sensor field-of-view. It was small when transmission was high, such as cold-air particles (relative to source). The spectral path radiance was then

$$L_{path}(\lambda) = [1 - t_{path}(\lambda)]L_{BB}(T_a) \left[\frac{W}{\text{cm}^2 \text{ Sr } \mu} \right] \quad (7)$$

where $t_{path}(\lambda)$ was the atmospheric transmission of the path and L_{BB} was the blackbody radiance of the atmosphere with a temperature T_a .²⁰ The attenuation up through infrared wavelengths is shown in Figure 9.

There are a number of models used to compute the amount of atmospheric attenuation. These include the MODerate resolution TRANsmission (MODTRAN) model, Standard High Altitude Radiation Code (SHARC) and the combined SHARC and MODTRAN Model (SAMM).

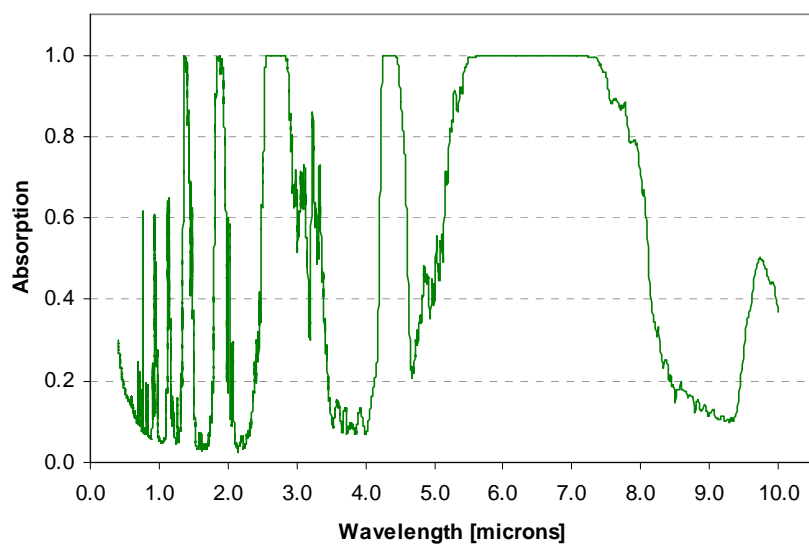


Figure 9. Visible and infrared atmospheric attenuation profile from PLEXUS

MODTRAN is the DoD standard atmospheric IR/VIS/UV radiance and transmission band model for lower altitudes (below 100 kilometers), developed and maintained by SSI and AFRL. MODTRAN rapidly predicts the atmospheric emission, thermal scatter, and solar scatter for arbitrary, refracted paths above the curved Earth, incorporating the effects of molecular absorbers and scatterers, aerosols and clouds. SHARC is a non-equilibrium high-altitude IR emission model for quiescent and aurorally disturbed atmospheres. SAMM is an all-altitude atmospheric IR model used by DoD. The SAMM code is a fully correlated coupling of the MODTRAN and SHARC atmospheric models, which predicts seamless path radiances for limb paths from 300 kilometers to the ground.

AFRL has built a modeling tool that incorporates the above three models into a user friendly interface. The Phillips Laboratory EXpert User System (PLEXUS) takes

user inputs as to the sensor and target position and calculates the path attenuation and radiance at the specified frequencies. An example output can be seen in Figure 10. The left panel shows spectral transmittance, while the right panel shows spectral radiance for the line-of-sight specified.

A drawback of using MODTRAN for space objects was that the algorithm was only useful to an altitude of 100 km in the visible spectrum. SAMM, on the other hand, was capable of handling all altitudes for infrared wavelengths greater than 1.4 microns. However, since the majority of attenuating atmosphere lies below 100 km, MODTRAN will be used. PLEXUS determines both the attenuation and the atmospheric path radiance along the line of sight.

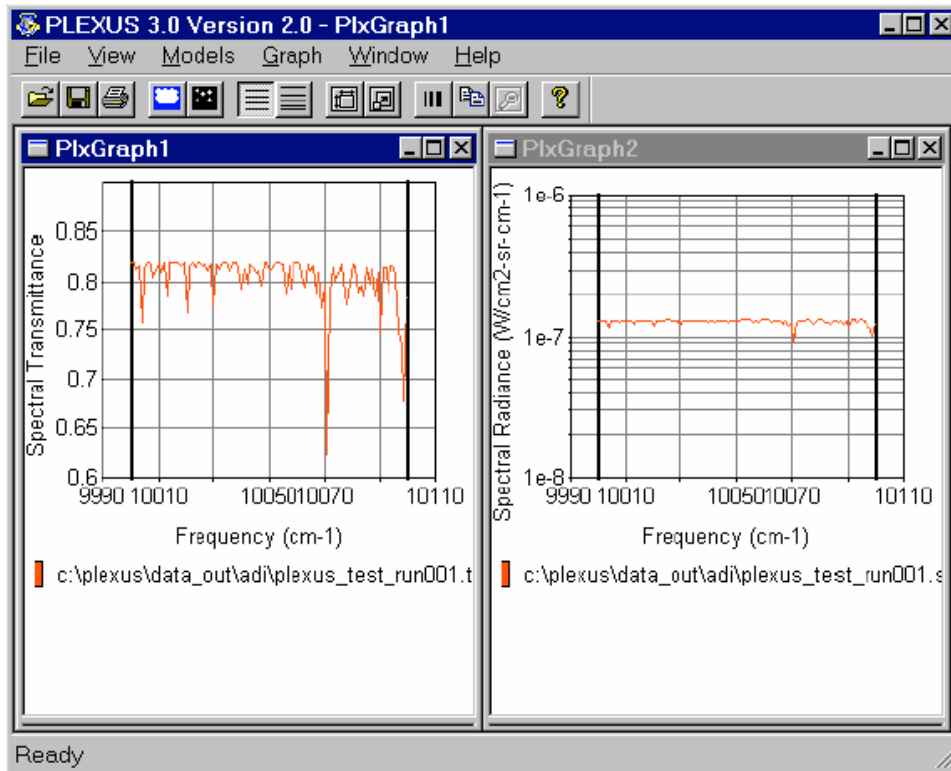


Figure 10. PLEXUS output display interface

The path between the ground observer and satellite must be evaluated for each satellite position. A secondary concern was if there was any atmospheric attenuation between the satellite and the sun. A quick analysis of the positions of the satellite and sun for each flare examined shows that the line of sight between the sun and satellite did not intercept the atmosphere. This would need to be accounted for if other reflection geometries were considered.

2.5 Iridium Satellite Constellation

The Iridium constellation of communication satellites are in near-polar orbits (86.4 degree inclination) at an altitude of approximately 780 kilometers (776 x 779 kilometers). The constellation was originally designed to consist of 77 satellites orbiting the Earth; its name was derived from the classical model of an iridium atom with 77 electrons ‘orbiting’ the nucleus. After a number of system reconfigurations and satellite and launch failures, the constellation shrunk to 66 active satellites plus on-orbit spares.

This orbital configuration provides the following benefits over systems based on other orbital configurations: no significant transmission delays; small, handheld pagers and phones; lower transmit power resulting in longer battery life; and complete global coverage, including all oceans and all land areas including the poles. Figure 11 shows an example of the constellation’s orbital planes and satellite positions.

Each satellite has three Main Mission Antennas (MMA’s) spaced evenly around the main satellite body. Figure 12 shows a picture of an Iridium satellite with two of the three MMA’s visible on the lower half of the satellite.

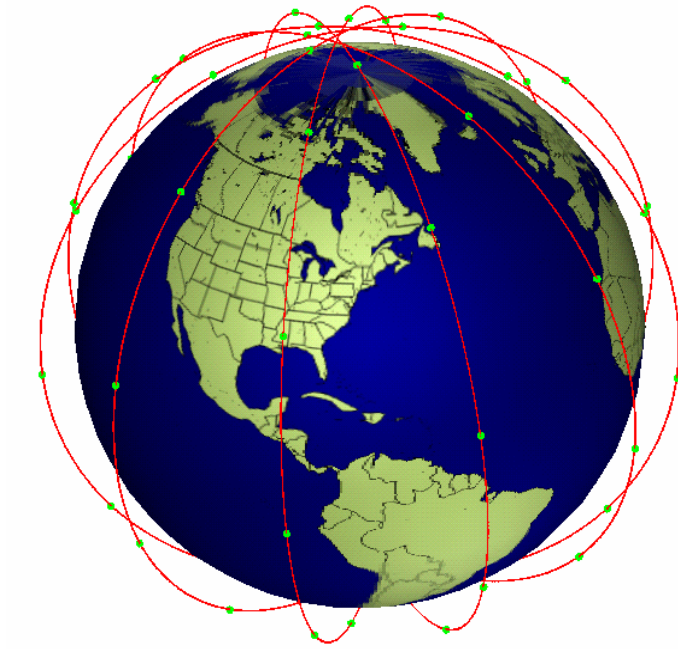


Figure 11. Iridium orbital planes²¹



Figure 12. Artist concept of Iridium satellite²²

2.6 Satellite Flares

Satellites are usually imaged in the visible or infrared. The irradiance of the satellite depends on a variety of factors. These include size, surface composition, sensor-satellite-sun geometry and atmospheric attenuation, among others.

Flares, also referred to as sun glints, occur when a particular satellite panel specularly reflects the sun's light close to a ground observer. This resulted in a temporary but rapid increase in the satellite's apparent brightness while the sensor was near the center of reflected beam. The footprint of the reflection moves rapidly across the ground as the satellites orbital motion carries it past the observer. The more specular the reflection off of the satellite, the narrower the beam and thus the more rapid an increase in the brightness. Figure 13 shows one of the earliest known images of an Iridium flare. The secondary 'flare' on the right side of the image was a reflection within the camera.



Figure 13. One minute exposure of Iridium 12 flare²³

2.6.1 Iridium Flares

Any satellite with smooth, flat surfaces can produce a flare, given the correct shape and sensor-satellite-sun geometry. Iridium was a particularly good satellite to observe since its orientation, shape and position are well known. Since, there are over 66 satellites with identical configurations, thus opportunities to observe are relatively common-place. Besides the number of available satellites to observe, there are several reasons that the Iridium constellation was good at producing flares.

The Iridium satellites are gravity gradient satellites. This means that with respect to the Earth, the satellite maintains its long (body) axis pointed toward the Earth, with its solar panels more or less perpendicular to this long axis. Gravity maintains this orientation throughout each orbit.

Each satellite was approximately 4 meters in length and 1 meter across. The communications payload consists of three MMA's, three smaller crosslink antennas and four small bronze gateway antennas. The two solar panels, spanning approximately 8 meters in length, track the sun while the spacecraft orbits the Earth.²⁴

The MMA's are spaced 120 degrees apart, around the satellite main body. These antennas receive and transmit phone calls from one Iridium handset to another. Each antenna has a fixed orientation at an angle of 40 degrees with respect to the long axis of the satellite. The satellite was also designed and operated such that one of the MMA's was always pointing along the orbital velocity vector.²⁵

It was needed to determine which surfaces on the satellite would reflect the sunlight. Amateur and professional satellite trackers have been reporting sun glints from

Iridium satellites shortly after the launch of the first satellites. It did not take long for the first glints to be confirmed.

2.7 Magnitudes and Flux

Telescopes usually measure a target signal flux. It is, however, common to compare the apparent brightness of an object with some known stellar objects. Measurements using this method are called magnitudes and are commonly used in astronomy. To convert between magnitudes and irradiance, the following equation is used:

$$m_v = -2.5 \log\left(\frac{f_{sat}}{f_{sun}}\right) - 26.8508 \quad (8)$$

where f_{sat} is the energy irradiance (sometimes referred to as flux by astronomers) in the visible spectrum of the object and f_{sun} is the solar constant over visible wavelengths.²⁶ The irradiance between 0.4 and 0.7 microns is 508 W/m². Magnitudes are used to compare unknown objects against stars with similar magnitudes. These calculations are made based upon the received flux (irradiance) at the top of the atmosphere.

2.8 Satellite model

The Iridium satellite was relatively small and had a simple shape. Figure 14 shows the basic Iridium satellite without solar panels. It is approximately 4-meter long three sided body. Each side of the body is approximately 1.25 meters in width. A sun-tracking solar panel, approximately 8 meters in length traverses the top end of the satellite. This model was used to determine the reflection angles and projected areas.

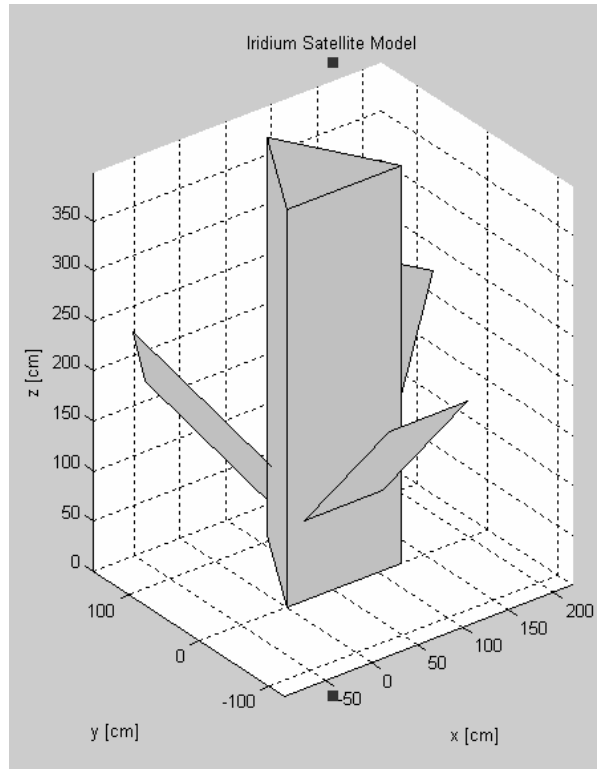


Figure 14. Iridium satellite model generated using Matlab[®] code in appendix 1

Modeling the reflected sunlight from a satellite could not be done unless detailed knowledge of the satellite's geometry was known. To determine the sensor-satellite-sun geometries, Satellite Tool Kit[®] (described below) was used to determine most of the satellite to sun and satellite to observer angles and distances. A satellite model was built using Matlab[®] in order to determine the scattering angles from the MMA's. The source code for this model is shown in Appendix 1.

2.9 Thermal Emissions

Reflections off of space objects are predictable when the objects geometry, attitude, and orbit are well known. Even in this situation, they tend to be relatively rare events. However, more often than not, the observer will not be favorably positioned to

measure the reflected sunlight.

More likely, the observer will need to rely upon the satellite's thermal emissions in order to detect the object. If the true temperature of an object is used, these emissions follow a strict Planck curve, with the peak defined by Equation (2).

Besides not requiring favorable geometry, thermal emissions have other differences from flares. BRDF's are no longer a concern for thermal emissions. This accounts for the nearly two orders of magnitude loss due to the specular nature of the materials involved.

Satellites have rigorous thermal control regimes to keep their internal and external temperatures in balance and at an operational level for delicate internal components. However, it was not possible to do this without some emissions from the satellite body. Thermal control is typically accomplished using heaters, radiators and thermal blankets. Radiators typically have emissivities near 0.8, whereas thermal blankets typically range from 0.1 on upwards. The temperature of each portion of a satellite is a function of the internal heat requirements, solar heating, and satellite orientation and geometry.

Spot 4 is a commercial French imaging satellite that is approximately 5.4 by 2 by 2 meters in size. The thermal control system is designed to keep this satellite at 20 °C. However, when sun lit, the outer layers of the thermal blankets can reach 80 °C.²⁷

Nuclear powered satellites, on the other hand, have operating temperatures ranging from approximately 300 K to 900 K. While there are a limited number of nuclear powered satellites currently in orbit, it was possible that future satellites may well be nuclear powered. Full sized nuclear reactors have large radiators, in the tens of

meters. The more common Radioisotope Thermal Generators (RTG) are typically one square meter in size.²⁸ This analysis will be limited to the larger nuclear reactors, as the RTG's have sizes and thermal characteristics that are in line with non-nuclear satellites.²⁹

Per Equation (2), the peak wavelength was a function of the temperature of the blackbody. For each body, a small spectral band was selected that minimized atmospheric attenuation. The characteristics used to analyze these thermal emissions are shown in Table 1.

Table 1. Thermal Emission Characteristics³⁰

True Temperature	Representative Object	Peak Wavelength [microns]	Spectral Band [microns]	Atmospheric Transmittance	Emission Source Size [m ²]
333 K	SPOT 4	8.21	8.05 – 8.51	0.73	2
900 K	Nuclear Reactor	3.22	3.1 – 3.71	0.57	20
1300 K	Reference	2.23	2.02 – 2.43	0.86	2

2.10 Summary

Satellites produce reflections when sunlit. These reflections can be observed if the geometry favors the observer. A material's BRDF determines its scattering characteristics and thus the amount of light reflected towards the observer. Atmospheric models determine the amount of the reflection that was attenuated, based on seeing conditions and wavelength. Thermal emissions, on the other hand, are a function of temperature and emissivity, and are also attenuated by the atmosphere. Based on this background, a detailed research methodology is described in the next chapter.

III. Methodology

3.1 Chapter Overview

The purpose of this chapter is to outline the methods used to measure the flares and emissions from various satellites.

3.2 Satellite in Field-of-View

The first step was to determine which satellites will be within the field-of-view (FOV) of a chosen ground sensor. The primary method for accomplishing this was to use the IRIDFLAR (v2.21) program by Rob Matson.³¹ IRIDFLAR generates predictions based on the users location during the time period specified. A secondary tool, www.heavens-above.com was also used to verify the accuracy of the IRIDFLAR data.

3.3 Orbit Determination

Next, it was needed to determine what orbit the satellite was in. This was done using the two-line element (TLE) set published by the Air Force Space Command. There are a number of websites that publish Iridium TLE's. The TLE was used by flare prediction software and orbit determination programs. See Appendix 2 for the Iridium TLE used.

3.4 Satellite Attitude Determination

Satellite attitude or orientation with respect to the sun and ground sensor varies by satellite design and operations mode. Simple satellites with omni-directional antennas and body mounted solar arrays typically do not require critical satellite pointing, and hence may spin with an unknown orientation and rate.

Generally, the more complex a satellite's mission, the more likely that it will require some sort of Earth pointing or other attitude control regime. The Iridium satellite has a particularly predictable satellite attitude.

The Iridium constellation is gravity gradient stabilized satellites. Thus, the 'heavy' end of the satellite points towards the Earth's center. In addition, the satellites three MMA's need to maintain a relatively fixed orientation with respect to the satellites orbit. The satellite, therefore, maintains one MMA's in the forward facing position with respect to the satellites orbital motion. Thus, at any given moment, the position of these sun-glinting MMA's was well known, making sun-glint predictions easier to do. Some objects do not have such careful attitude control regimes, however.

There are a number of objects in Earth orbit which are either dead / decommissioned satellites or spent rocket bodies. Careful observations of some of these objects can yield some knowledge about their pointing and spin rates. Magnitude studies show a magnitude versus time trend emerges for some objects that are in a controlled and/or recurring attitude management scheme. This technique was used to derive the flare predictions used in the IRIDFLAR program.

Paul Maley of NASA Johnson Space Center has reported that once each Iridium satellite reaches its parking orbit, its orientation relative to its velocity vector was maintained to within +/- 0.5 degrees in pitch, +/- 0.4 degrees in roll and +/- 0.5 degrees in yaw. If orientation errors conspire in a worst-case fashion, the minimum flare angle (a.k.a. mirror angle) for a particular pass can increase by as much as 1.4 degrees (two times the root-sum-square of 0.5 and 0.5). This could change the brightness of a best-

case pass by almost seven orders of magnitude (changing flare angle from 0 to 1.4). The effect on the magnitude was not as severe for larger flare angles; for example, a change from 1.0 to 2.4 decreases the theoretical brightness by only 2.3 visual magnitudes.³²

Since the satellite orientation errors cannot be known a priori, it is not possible to reliably predict which flares will be absolute "show stoppers." Of course, orientation errors can either improve or degrade the magnitude of the actual observed flare. A predicted flare angle of 1.5 degrees could conceivably be improved to 0.1 degrees, transforming a medium brightness flare into a -8 magnitude flare.³³

3.5 Satellite Geometries

The projected areas with respect to the ground sensor and the sun need to be determined in order to find how much reflected sunlight reaches the sensor. Complex models may involve multiple surfaces, materials and optical paths. Some reflected light may reflect off of one or more other satellite surfaces before traversing the atmosphere to the sensor. These multiple reflections should normally be accounted for.

However, due to the Iridium satellite's somewhat unique geometry calculations for multipath to the ground sensor could be largely ignored. This was primarily because of the mostly specular BRDF of the MMA's and their geometry.

Iridium's MMA's are made from highly reflective aluminum flat plates (treated with silver-coated teflon for thermal control) that are angled 40 degrees away from the axis of the body of the satellite.

While the main satellite body is coated with reflective mylar strips, the positioning of the MMA's blocks most of this light, except in situations where the

satellite was low in the sky and the sun was in the opposite direction. This would lead to near normal angles from the sensor to satellite and satellite to sun. However, in this orientation, an MMA would be blocking the lower half of the satellite body, reducing the reflected light. At intermediate orientations, the MMA's would not be blocking the sunlight, but the projected area was significantly smaller, reducing the amount of reflected light seen by the sensor. Thus, the vast majority of observed reflected light was from the front side of the MMA's.

3.5.1 Sun-Satellite and Satellite-Sensor Geometry

Once the satellite's attitude was known, the projected cross-sectional area of the satellite, with respect to the sun, could be determined, given a sufficiently robust satellite model. This was determined by taking the normals of each satellite panel and finding the angle between that normal and the satellite-sun and satellite-sensor line. The projected area was then the cosine of the angle times the area of the panel.

3.5.2 Satellite Tool Kit

Analytical Graphics Incorporated's Satellite Tool Kit[®] (STK) was a useful tool for calculating satellite geometry. STK will calculate a variety of geometric measurements. Satellites can be loaded from the installed database, from a TLE file (see Appendix 2), or entered by hand. The installed database can be updated through STK's online update feature. TLE's for any unclassified satellite can be downloaded from Air Force Space Command website. Specific groupings of TLE's for a variety of satellite constellations or groupings can be obtained from a number of websites.³⁴ However, due to recently passed laws³⁵, Air Force Space Command will become the sole distributor of

TLE's. It is unlikely that TLE's for many satellites will be available on these websites after Air Force Space Command has fully implemented its program.

Generating all the required vectors and angles for each satellite on each predicted pass and for each site was a protracted process. Each satellite must be positioned for the predicted flare time. STK has a number of built-in vectors that point to/from the satellite, sun and ground sensor. However, many of the angles between these vectors need to be verified for accuracy prior to use. STK has a built-in geometry tool that can be used to determine the angle between two vectors, a vector and plane, two planes, and even between two vectors, about a third vector, taking the direction into account. This was a rather involved and time consuming process for new users to STK. This process must be repeated for each satellite, site and time. There are some streamlining methods that can be used to speed this process along (e.g., keep angles and adjust time before switching to site angles/vectors). Overall STK was a valuable tool for generating data regarding satellite geometry despite its sometimes steep learning curve.

3.5.3 Units

Given the number of different software tools used, there were a number of unit differences that needed to be accounted for.

STK's vector geometry tool can be used to generate azimuth and elevations instead of right-ascension / declination. The magnitudes of these angles were the same, but the sign of the angle, due to choice of the vector of rotation, was different. Care had to be taken in order to account for sign conventions and the vector of rotation, but otherwise the geometry tool is a fairly straightforward method of checking angles. Once

generated, the azimuth and elevation vectors and angles were used to calculate the sun-satellite-sensor geometry.

3.6 Numerical Process

The overall process of determining the flare radiance consists of several steps: positioning the satellite, calculating satellite geometry, determining the projected area of the MMA, measuring spectral reflectance, figuring the scatter angle and establishing how the atmosphere attenuates the signal. The specifics of each step are outlined in the following paragraphs.

The Matlab[®] Iridium satellite model was used to determine the angle between the normal of the MMA and the sun vector and similarly between the MMA normal and ground observer. This was then used to determine the angle between the reflection vector and the vector from the satellite to the ground station.

As a confirmation of the data obtained using STK, the Matlab[®] model was used to provide a crude estimation as to the accuracy of our angles. This was done by specifying the ground site as the point-of-view for the model and placing a light source at the position of the sun. With the model reflections turned on, the brightness of the panel in question increases towards white as the flare angle was reached. This indicates that the correct reflection angles have been achieved, since the light source was now reflecting towards the observer. This check caught several data entry errors during the calculations process.

3.6.1 Panel Projected Area

For reflections, the projected area of the panel effectively acts like an aperture

stop for the ground sensor. The solid angle subtended by the panel affects how much of the source, the sun in this case, can be seen by the sensor. Using the Matlab[®] Iridium model discussed in Section 2.8, the angle between the sensor-satellite line and the normal of the MMA is computed. The projected area was then easily determined from this angle. The majority of the Iridium flares were reflections from the MMA on the left side of the satellite as defined by the satellites forward motion. The left MMA tended to have a good portion of the MMA visible to the ground observer. Given a panel real area of approximately 1.62 m², the typical left MMA projected areas tended to be between 1.20 m² and 1.40 m². On the other hand, early morning daylight flares tended to be caused by the right-side MMA, which generally had a much smaller projected area of around 0.1 m² to 0.5 m². This added to the difficulty of detecting daytime flares.

3.6.2 Spectral Reflectance

As stated earlier, a material's reflectance depends on the geometry and wavelength of the incident light. Figure 15 shows the specular reflectance of aluminized kapton and aluminized mylar in the visible. It also shows the average reflectance of the two materials. As was seen in the figure, between 0.4 microns and 0.5 microns there was significant difference in the reflectivity of aluminized kapton and aluminized mylar. Above 0.6 microns the reflectance of the two materials are quite similar.

Figure 16 shows the post effect of applying this reflectance data to the solar Planck curve. For the band used in the flare calculations (0.4 to 0.7 microns), the radiance varied from 332.9 W/cm²-Sr for aluminized kapton to 620.7 W/cm²-Sr for aluminized mylar, with a value of 476.8 W/cm²-Sr for the average reflectance.

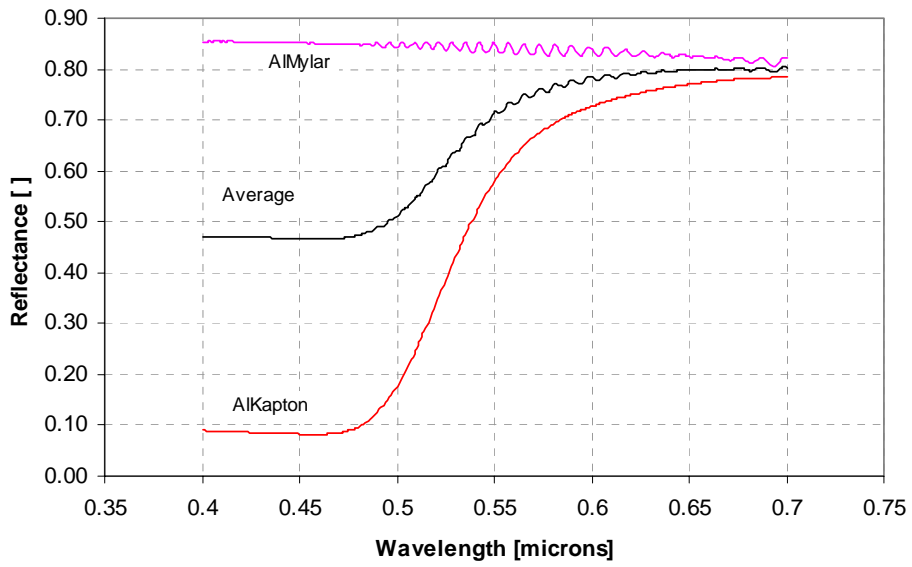


Figure 15. Reflectance of aluminized kapton and mylar³⁶

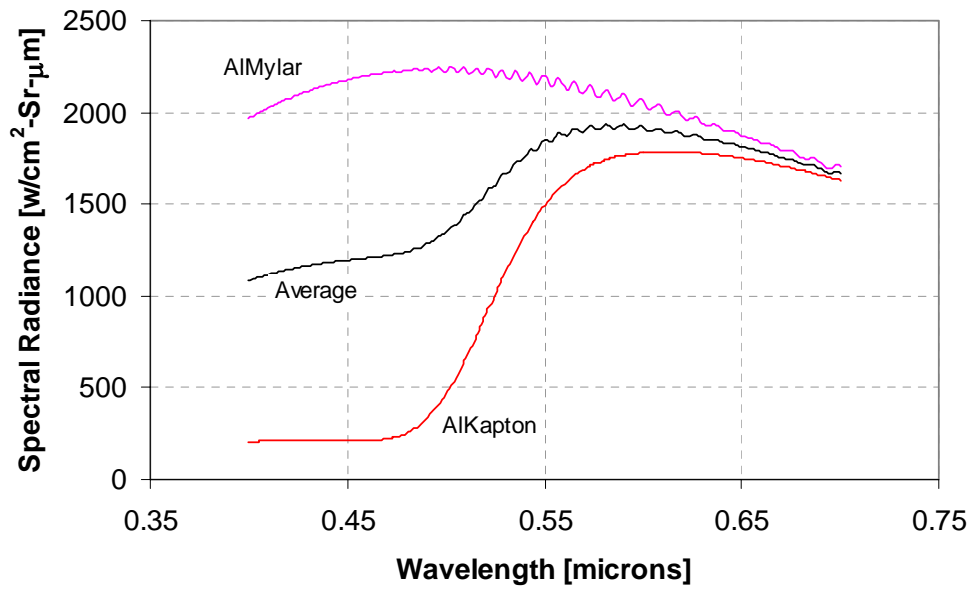


Figure 16. Solar radiance reflected off of satellite main mission antennas

3.6.3 Silvered Teflon and Aluminized BRDF's

Besides the spectral nature of the material reflectances, we must also consider the materials bi-directional distribution functions. As can be seen in Figure 17, these materials are for the most part highly specular. Any non-specular reflection from the aluminized kapton falls off by two orders of magnitude within 1.5 degrees of the classical specular reflectance angle. A three-order magnitude drop off occurs by 4.5 degrees.

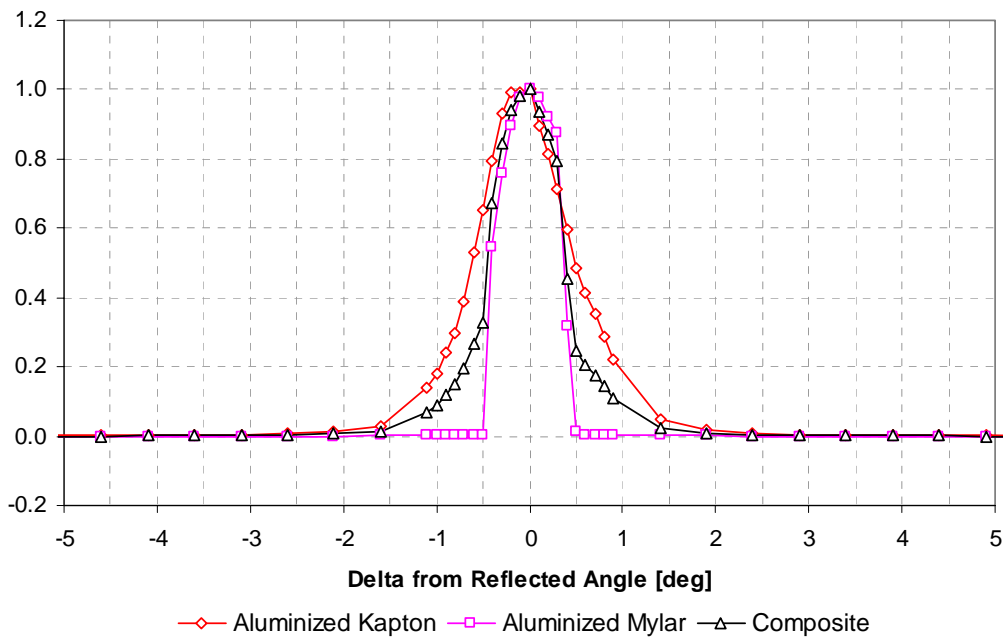


Figure 17. Normalized BRDF's from Optical Measurement Facility data

For aluminized mylar, the fall-off was even more dramatic. Two orders of magnitude drop-off can be found at 0.5 degrees off of the expected specular angle. 0.1 of a degree further from the specular reflectance angle, the fall-off increases to three orders of magnitude.

Despite the nearly specular nature of the materials, the small angle scattering must

be taken into account. At slant ranges approaching 1000 kilometers or longer, even a deviation of 0.5 degrees from the reflected angle would amount to a ground distance of approximately 9 kilometers and a radiance fall off near 80%. The difference in angular position between the reflection point on the Earth's surface and that of the observer must be calculated and applied to the BRDF calculations.

3.6.4 Atmospheric Attenuation

PLEXUS was used to determine the amount of spectral attenuation and also the path radiance for each satellite. PLEXUS was used in the Novice/Casual user mode, given that there were not too many parameters that needed to be altered. Besides observer and satellite location, other parameters entered included: clear day with high visibility (50 kilometers), maritime environment (Maui) and no significant weather in the previous 24 hours. These were the default values for most runs. Some comparisons were also conducted for slightly lower visibilities (23 kilometers).

PLEXUS also determines the path radiance along the line of sight from the observer to the target. This was applied against the FOV of the ground sensor to determine the background irradiance. It was assumed that the background was uniform across the FOV of the sensor, except at the position of the satellite.

3.7 Thermal Emissions

Thermal emissions are a function of body temperature and emissivity. Using Planck's Radiation Law, Equation (1) with the true temperature to account for the emissivity, the radiant output of an object was calculated. This was then applied against the atmospheric attenuation and projected panel size to find the received irradiance.

The sun was the source for the reflected flares. For thermal emissions, however, a space object is the source that drives the irradiance measured. By Kirchoff's Law, $\varepsilon = 1 - \rho$. Using BRDF's to determine the emissivity, the angular dependence would have to be considered. However, since radiators on spacecraft are designed to dump as much heat as possible, in all directions, we can treat the radiator as a Lambertian emitter, ignoring any angular dependence. Thus, the spectral reflectances and BRDF's were eliminated from the calculations.

3.8 Signal-to-Noise Ratios

In Equation (5), there are a number of terms that needed to be defined for these calculations. The quantum efficiency, η , was set at a very efficient value of 1. The area of the detector, A_d is set at 3.14 m^2 (2 meter diameter telescope), and the noise-equivalent bandwidth, Δf , is set to 1 Hz. The values for quantum efficiency and noise-equivalent bandwidth are best case values. They represent the most optimal conditions for detectivity possible. Real world values will differ from these numbers.

3.9 Problems Encountered

There were a number of problems that were encountered during the course of this thesis. These included data processing, PLEXUS limitations and logistical problems.

The abundance of data was primarily due to the number of different programs used to develop and implement this model. Preliminary solar radiance calculations were done using Mathematica[®]. Matlab[®] was used for the Iridium model, finding panel projected areas and angles between the reflected vector and site vector. This model was also used to verify the predicted flares. STK was used to find all other angles. PLEXUS

was used to determine the spectral transmission of the atmosphere, wavelength by wavelength. The spectral reflection data and BRDF's were provided in an Excel[®] format. Excel[®] was also used to pull all this data together, mesh the various formats and scales and conduct final number crunching.

Matlab[®] would likely be the best tool in the future for many of these calculations. STK has a Matlab[®] interface. The data from PLEXUS could easily be imported into Matlab[®]. Matlab[®] was capable of handling all calculations and data manipulations used in Excel[®].

Another problem encountered was that PLEXUS only handles visible wavelengths below 100 kilometers. Attenuation calculations for higher altitude are only done for wavelengths above 1.4 microns. It was determined, however, that this impact on the attenuation would be relatively minor compared to the attenuation from the thick atmosphere below 100 kilometers.

3.10 Summary

Satellites that were within the FOV of each of these sites were modeled with STK. Satellite geometry was calculated using STK and the Matlab[®] model. Spectral reflectance values and BRDF's were applied to determine the spectral radiance. The projected area of the reflecting MMA was also calculated. Atmospheric attenuation was determined by the PLEXUS. The received irradiance was determined for each examined flare and compared against the path radiance along the line of sight. The next chapter reviews the results achieved using the process described above.

IV. Analysis and Results

4.1 Chapter Overview

The initial results for this thesis were aimed at validating the model against predicted Iridium flares. The model was also tested against simulated reflections. A variety of geometry and reflection conditions were used when testing artificial satellites in an orbit similar to Iridium satellites. The results of this further testing are also presented here. Finally, thermal emissions are examined in this chapter.

4.2 Iridium Flare Results

Iridium satellites that were predicted to flare between 4 and 14 November 2004 were studied in detail for this thesis. The predictions for the Maui site (latitude 20.7083° N, longitude 156.2581° W, elevation 3058 m) are shown in Table 2.

Table 2. IRIDFLAR predictions for Maui

Iridium Satellite #	Date	UTC Time	Azimuth [deg]	Elevation [deg]	Range [km]
10	11/4/2004	15:26:33	342	46	1036.2
40	11/5/2004	05:07:13	173	34	1248.7
13	11/5/2004	15:20:31	343	45	1041.5
17	11/6/2004	05:01:09	172	34	1248.1
50	11/6/2004	15:14:30	345	45	1050.3
82	11/7/2004	04:55:05	171	34	1248.7
53	11/7/2004	15:08:29	346	44	1063.4
43	11/11/2004	04:39:54	183	35	1228.5
40	11/12/2004	04:33:48	183	36	1217.4
17	11/13/2004	04:27:42	182	36	1206.6
72	11/13/2004	17:08:38	126	20	1734.3
83	11/14/2004	02:45:05	228	28	1407.9
80	11/14/2004	16:28:43	355	67	832.8
75	11/14/2004	16:42:21	92	17	1899.9

Two flares, a nighttime Iridium 40 flare on 5 November, 2004 and a daytime

Iridium 72 flare on 13 November, 2004, were analyzed further.

4.2.1 Iridium 40 Nighttime Flare

This particular flare was predicted to occur at 05:07:13 UTC (19:07:13 local) on the 5 November (UTC, 4 local). At that time, the Iridium 40 satellite was located at an azimuth of 176.59 degrees, altitude of 42.58 degrees and a slant range of 1248.61 kilometers from the Maui site.

The resulting irradiance was calculated to be $3.36 \times 10^{-8} \text{ W / m}^2$. The background irradiance for a 1 degree FOV (FOV) was calculated to be $2.843 \times 10^{-34} \text{ W / m}^2$. The flare was clearly visible with this FOV. The radiance of the night sky, as predicted by PLEXUS was not sufficient to overcome the flare radiance. Seeing conditions were optimized for clear visibility (23 kilometers) and a maritime aerosol environment. Table 3 shows the results of several samples taken before, during, and after the predicted Iridium 40 flare on 5 November 2004. The table shows the irradiance for aluminized kapton, aluminized mylar and the average of the two materials.

Table 3. Iridium 40 nighttime flare irradiance

UTC	Azimuth [deg]	Elevation [deg]	Slant Range [km]	Flare Irradiance [w/cm^2]		
				AlKapton	AlMylar	Composite
05:06:13	167.17	51.62	958.82	7.83E-12	3.15E-13	5.58E-12
05:06:43	170.61	41.89	1093.147	3.46E-10	5.43E-10	4.52E-10
05:06:53	171.38	39.11	1143.03	1.65E-10	6.22E-11	1.39E-10
05:07:03	172.04	36.55	1194.934	1.43E-11	2.22E-13	9.95E-12
05:07:13	172.6	34.17	1248.608	4.78E-12	1.61E-13	3.36E-12
05:07:23	173.09	31.96	1303.83	8.95E-13	9.34E-14	6.52E-13
05:07:33	173.53	29.91	1360.39	3.61E-13	6.71E-14	2.74E-13
05:07:43	173.91	27.99	1418.462	2.05E-13	5.02E-14	1.60E-13
05:08:03	174.56	24.54	1536.64	7.42E-14	2.86E-14	6.17E-14

IRIDFLAR predicted a flare at 05:07:13 with a magnitude of 0.4 at the site, and a peak of -7.4 for an observer located at the flare scattering angle. The computed magnitudes are shown in Table 4.

Table 4. Iridium 40 Nighttime Flare Magnitudes

UTC	Magnitude		
	AlKapton	AlMylar	Composite
Zero Attitude Error			
05 Nov 04 05:06:13	-2.5	0.9	-2.2
05 Nov 04 05:06:43	-6.7	-7.2	-7.0
05 Nov 04 05:06:53	-5.9	-4.9	-5.7
05 Nov 04 05:07:03	-3.2	1.2	-2.9
05 Nov 04 05:07:13	-2.1	1.5	-1.7
05 Nov 04 05:07:23	-0.3	2.1	0.0
05 Nov 04 05:07:33	0.7	2.4	0.9
05 Nov 04 05:07:43	1.3	2.7	1.5
05 Nov 04 05:08:03	2.3	3.3	2.5
-1.4 deg Attitude Error	AlKapton	AlMylar	Composite
05 Nov 04 05:06:13	-0.1	1.5	0.1
05 Nov 04 05:06:43	-2.9	1.1	-2.5
05 Nov 04 05:06:53	-5.0	0.9	-4.6
05 Nov 04 05:07:03	-6.5	-7.0	-6.8
05 Nov 04 05:07:13	-5.6	-2.1	-5.3
05 Nov 04 05:07:23	-3.0	1.4	-2.7
05 Nov 04 05:07:33	-1.9	1.8	-1.5
05 Nov 04 05:07:43	-0.9	2.0	-0.6
05 Nov 04 05:08:03	1.0	2.8	1.2
+1.4 deg Attitude Error	AlKapton	AlMylar	Composite
05 Nov 04 05:06:13	-6.3	0.3	-6.0
05 Nov 04 05:06:43	-4.5	0.9	-4.1
05 Nov 04 05:06:53	-2.4	1.3	-2.1
05 Nov 04 05:07:03	-0.5	1.9	-0.2
05 Nov 04 05:07:13	0.5	2.2	0.7
05 Nov 04 05:07:23	1.1	2.5	1.3
05 Nov 04 05:07:33	2.0	3.0	2.2
05 Nov 04 05:07:43	2.9	3.4	3.0
05 Nov 04 05:08:03	3.1	3.6	3.2

As can be seen in Table 4, the magnitudes varied by material and times from the predicted value. Ignoring the times, the calculated peak values were all brighter than the

predicted value. Differences in sensor-satellite-sun geometry may account for these variations, however. In general, these calculated values tended to predict brighter flares than those predicted by IRIDFLAR. A brief conversation with the IRIDFLAR programmer, Rob Matson, indicates that the methods used to calculate these predictions are quite different. There are no known studies that have compared how close the IRIDFLAR predictions were to actually observed flare magnitudes. There was confidence, however, that the predicted flare times are fairly accurate, to within minutes of the actual event. This was corroborated by visual satellite observers and matches the behavior of the data presented in Figure 18.

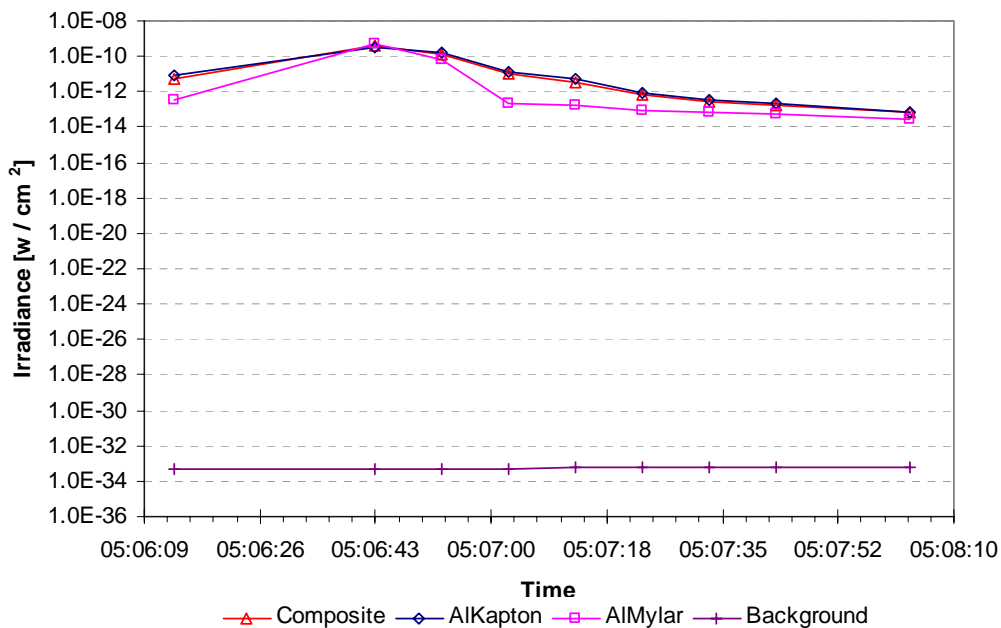


Figure 18. Iridium 40 flare

The Figure 18 shows the flare irradiances as the satellite passes through the peak flare position. Background visibility for this calculation was set at 23 kilometers of good

visibility. The IRIDFLAR prediction had the peak at 05:07:13 while the calculated values had the peak near 05:06:43. Both used the same TLE. Not having access to the IRIDFLAR algorithm prohibited discovering the discrepancy between the two results.

As mentioned previously, the uncertainty in the pointing of the satellite was ± 1.4 degrees. This error may result in significant ground track error. This causes the flare center to move either towards or away from the observer, resulting in significant changes in the irradiance. Taking the pointing errors into account, it can be seen from Figure 19 how this might affect the observed flare. The composite material from Figure 18 is the bold line with a peak at 05:06:43. The other lines show the effect of attitude errors; altering the peak irradiance and shifting the time of the peak forwards or backwards.

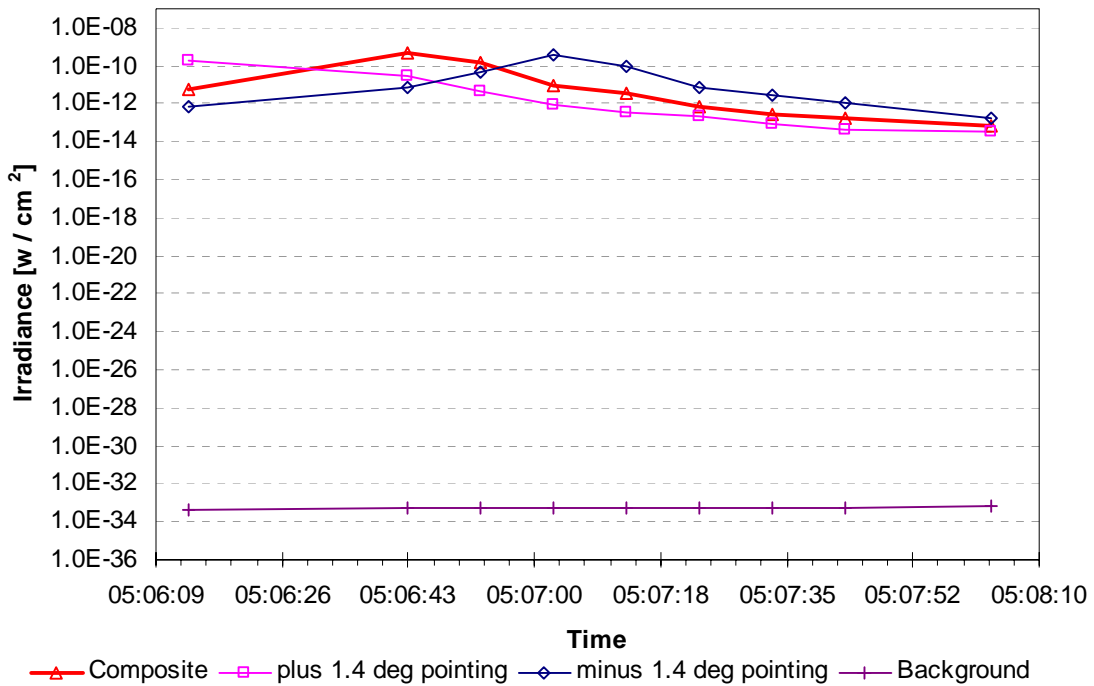


Figure 19. Iridium 40 flare irradiance due to pointing errors

Figure 20 compares the magnitudes of the calculated flares with that of the predictions. There was a significant difference in the magnitudes, though the peak values are close in time. Given the unknown spectral reflection and BRDF characteristics of the silvered teflon, this was within the realm of error. As stated earlier attitude errors, can change the predicted flares by up to seven magnitudes. Also note that there is no background magnitude shown. Magnitudes were originally designed for comparisons against stars in the night sky, thus they are a measurement of the objects irradiance at the top of the atmosphere. From Equation (8), the magnitude is a comparison of one object's irradiance to that of another. Thus, the magnitudes are compared to other known objects in the sky under the same seeing conditions, negating the need to determine what the background conditions actually are.

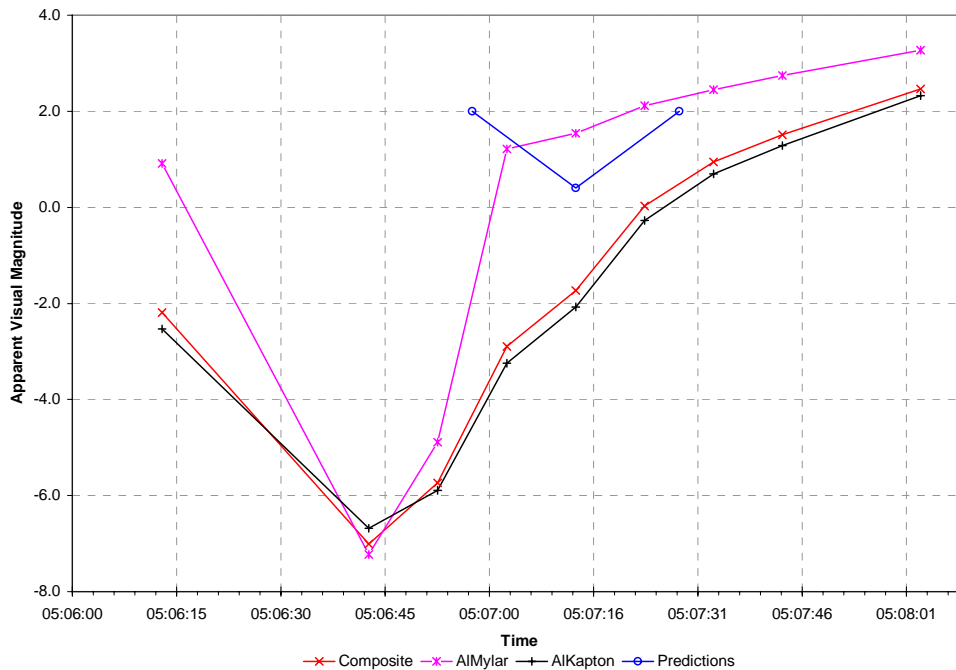


Figure 20. Magnitude of nighttime flare vs. predictions

Figure 21 shows the effect of attitude errors on the peak flare position. The SNR is evaluated in Figure 22. The flare is clearly detectable through the pass, as would be expected for a nighttime flare. The peak SNR was 6.05×10^{18} .

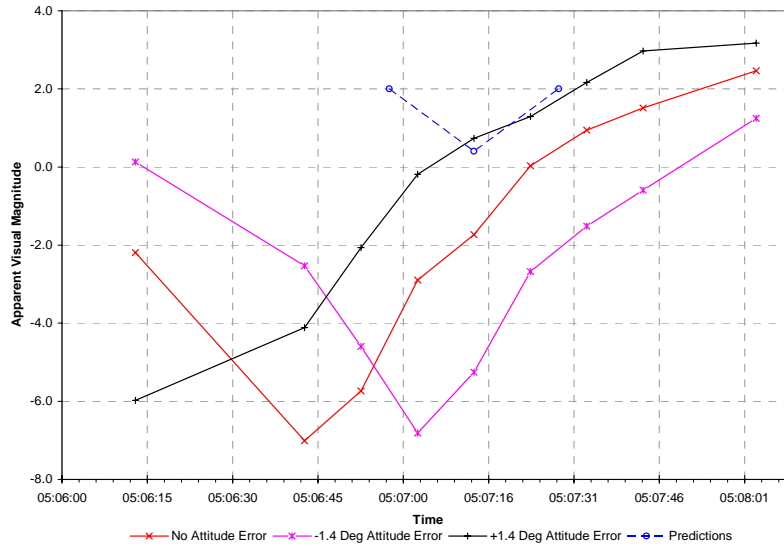


Figure 21. Effect of attitude errors on nighttime flare magnitude

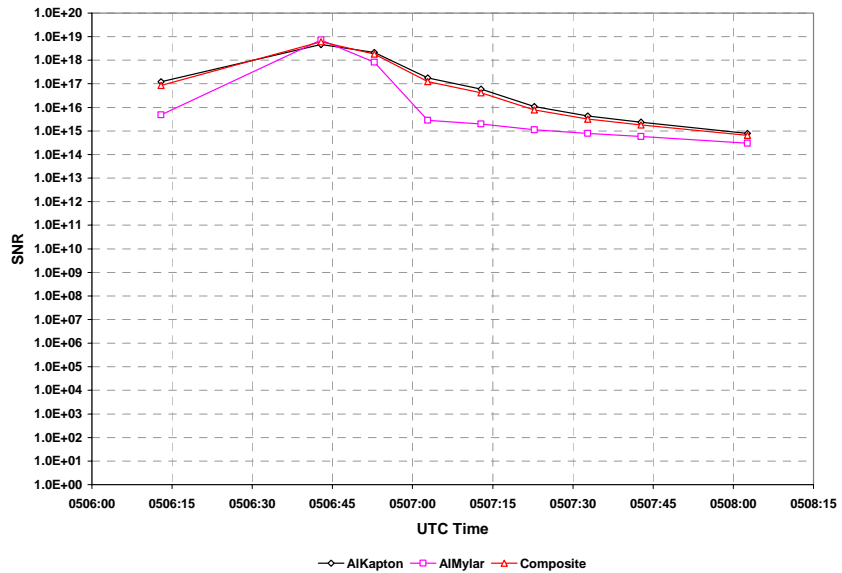


Figure 22. Nighttime flare SNR

4.2.2 Iridium 72 Daytime Flare

Iridium 72 was predicted to produce a daytime flare at 17:08:38 UTC on 13 November 2004. The satellite was located at an azimuth of 126.69 degrees, altitude of 19.7 degrees and a slant range of 1739.3 kilometers.

The resulting irradiance was calculated to be $3.23 \times 10^{-7} \text{ W/m}^2$. The background irradiance for a 1 degree FOV was calculated to be $7.625 \times 10^{-3} \text{ W/m}^2$. The daytime flare irradiance was not significantly different from the nighttime flare. The daytime background irradiance was, however, a great deal higher than the nighttime background irradiance. Table 5 shows the irradiance results for before, during and after the peak of the flare. The calculated peak of the flare occurred at 17:08:38 UTC, matching the IRIDFLAR prediction.

Table 5. Iridium 72 Daytime Flare Irradiance

UTC	Azimuth [deg]	Elevation [deg]	Slant Range [km]	Flare Irradiance [w/cm ²]		
				AlKapton	AlMylar	Composite
17:07:38	112.46	24.51	1538.52	2.467E-15	1.536E-15	2.287E-15
17:08:08	120.13	22.21	1628.76	3.700E-14	6.741E-15	2.775E-14
17:08:18	122.44	21.39	1663.54	1.940E-13	1.179E-14	1.360E-13
17:08:28	124.62	20.55	1700.43	5.182E-12	2.158E-14	3.509E-12
17:08:38	126.69	19.7	1739.3	2.412E-11	4.034E-11	3.229E-11
17:08:48	128.64	18.85	1780.02	3.539E-12	2.069E-14	2.388E-12
17:08:58	130.49	18	1822.45	7.675E-13	1.721E-14	5.217E-13
17:09:08	132.23	17.15	1866.47	1.575E-13	1.271E-14	1.104E-13
17:09:38	136.91	14.65	2007.00	9.029E-15	4.505E-15	7.790E-15
17:10:38	144.23	9.98	2317.82	8.383E-16	9.779E-16	9.395E-16

Figure 23 compares the calculated flare's irradiance against the background sky for a sensor with a 0.01 degree FOV. This flare was not visible as calculated.

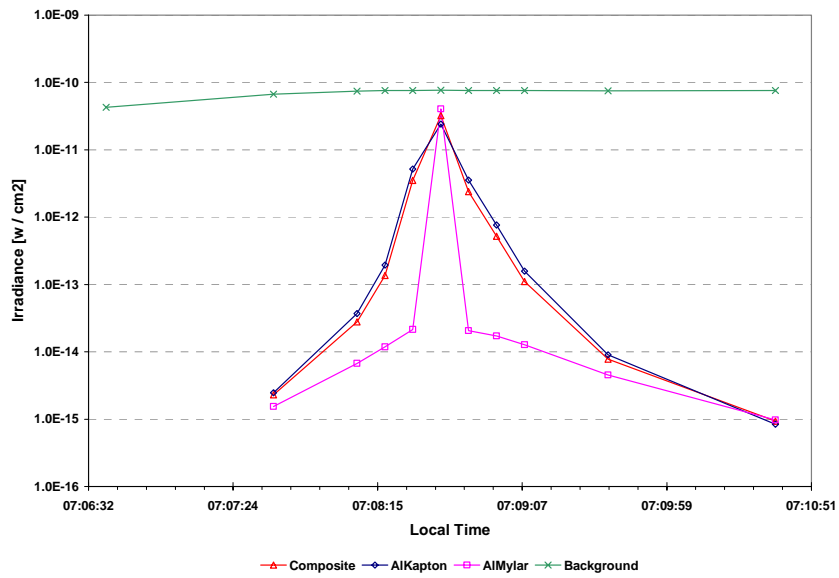


Figure 23. Iridium 72 flare with 0.01 degree field-of-view

Figure 24 compares the magnitudes from IRIDFLAR with those calculated. It was estimated that the discrepancies between the two sets of magnitudes are the result of attitude errors and the unknown spectral and scattering nature of silvered teflon.

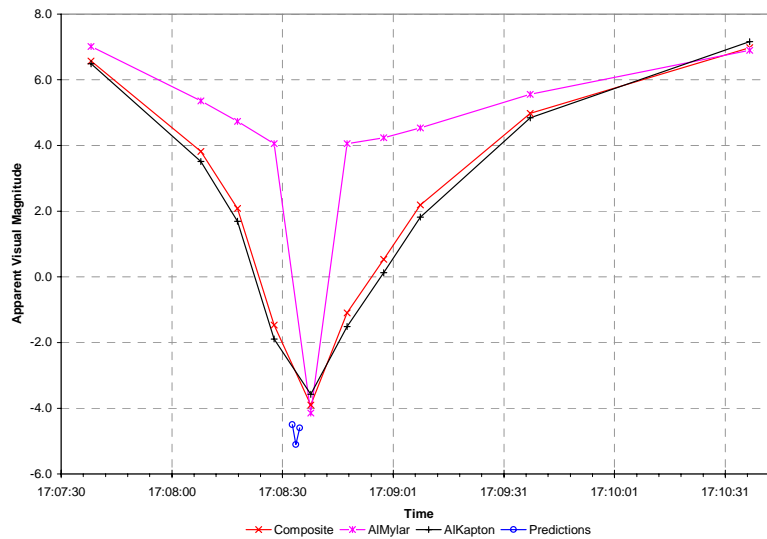


Figure 24. Magnitude of daytime flare vs. predictions

During this daytime pass, the sun was as close as 17.4 degrees from the satellite's position as viewed by a ground observer. The sun's position can obviously alter the background irradiance significantly. Using PLEXUS, the background irradiance was checked at angles up to 80 degrees from the sun's position. An examination of the data in Table 6 shows that both the slant range between the observer and satellite and the flare angle (between the satellite and the sun about the observer's position) affect the background irradiance. Regardless, the change in the background irradiance was not significant enough to see the daytime flare, which was only about 0.01% of the background at its peak.

Table 6. Background Irradiance as a function of slant range and flare angle

Local Time	Slant Range [km]	Flare Angle [deg]	Background Irradiance [w/cm²]
7:02:18	2168.4	80.07	2.01E-07
7:04:48	1544.9	54.08	2.15E-07
7:05:18	1476.8	46.92	2.43E-07
7:05:48	1435.9	39.4	2.89E-07
7:05:58	1428.7	36.89	3.10E-07
7:06:08	1424.9	34.4	3.33E-07
7:06:18	1424.5	31.97	3.60E-07
7:06:38	1433.8	27.36	4.24E-07
7:07:38	1538.5	18.03	6.66E-07
7:08:08	1628.8	17.35	7.44E-07
7:08:18	1663.5	17.71	7.55E-07
7:08:28	1700.4	18.29	7.61E-07
7:08:38	1739.3	19.05	7.62E-07
7:08:48	1780.0	19.94	7.61E-07
7:08:58	1822.5	20.91	7.60E-07
7:09:08	1866.5	21.95	7.57E-07
7:09:38	2007.0	25.21	7.51E-07
7:10:38	2317.8	31.45	7.58E-07

The SNR for a sensor with a 0.01 degree FOV are shown in Figure 25. The peak

SNR was $9.63e5$. While the SNR is above the detection threshold, these SNR's should be taken with a grain of salt. The Signal-to-Background Ratio (SBR) is below one, even at its peak. The SNR's were calculated using best case conditions and ignored other noises sources. Introduction of other noises sources would decrease the SNR significantly.

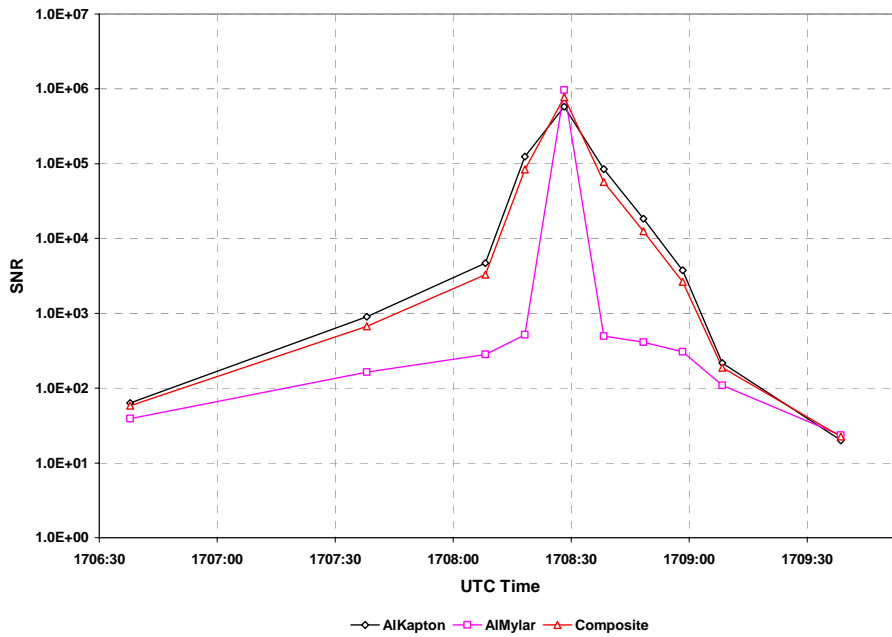


Figure 25. Daytime flare Signal-to-Noise Ratio (0.01 deg FOV)

4.2.3 Simulated ‘Flare’ Results

Flares are relatively rare occurrences for any given site. It was of interest however, to simulate these flares for a variety of sensor FOV's and panel reflectance characteristics. This section will deal with the analysis of the preceding daytime flare radiance using a variety of simulated satellite geometries.

Figure 26 shows the effects of various reflecting areas and BRDF's. Two

reflecting areas were chosen at 1 and 2 m². These reflecting areas are the effective or projected areas with respect to the ground observer. This area could be due to a variety of space object geometries, though this sets the minimum size of the object in the case of a direct reflection to the ground observer.

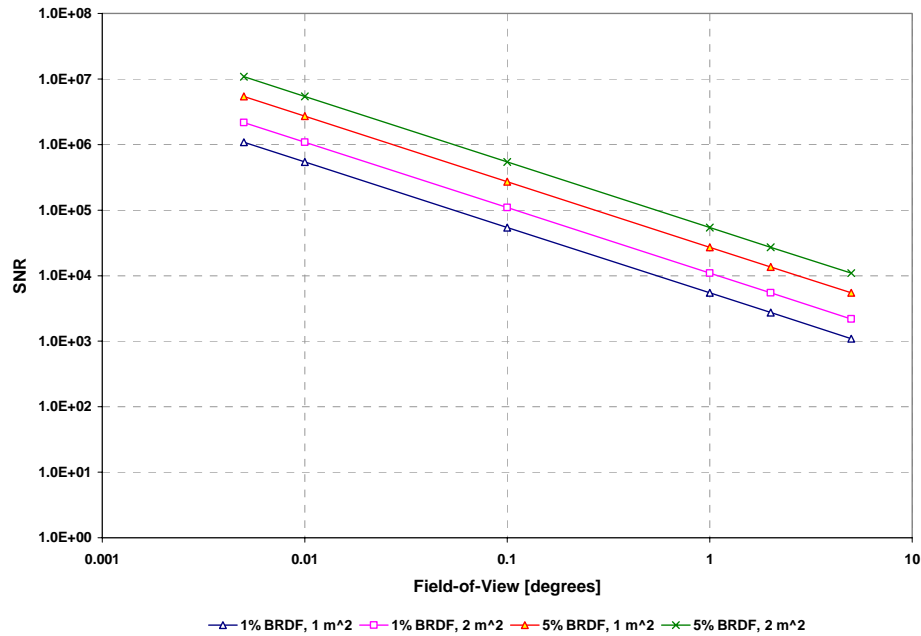


Figure 26. SNR for miscellaneous flares geometries

BRDF's are a function of the material, the incident angle and the scattering angle. The BRDF used in the calculations shown in Figure 26 used the composite values of the aluminized krypton and the aluminized mylar materials. As can be seen here, for this scenario, the BRDF has a greater impact than the increase in the reflecting area. This should be expected since the used materials were highly specular.

Increasing the slant range increases the background radiance significantly. A satellite in an 830 kilometer orbit had a slant range that varies between 830 to near 2850 kilometers. The background radiance changes by nearly two orders of magnitude ($6 \times 10^{-}$

$6 \text{ w/cm}^2\text{-Sr}$ at 800 kilometers to $6 \times 10^{-4} \text{ w/cm}^2\text{-Sr}$ at 2850 kilometers). Thus, there was a balance between the reflecting area, material reflectivity, and background irradiance.

4.2.4 Infrared Flares

Iridium flares are normally observed by amateur satellite spotters in the visible. However, sensors attempting to detect space objects during the day would not be limited to visible wavelengths. Infrared sensors can also detect the Iridium flares reflected from the satellite. This portion of the electromagnetic spectrum provides some advantages and some disadvantages over visible wavelengths.

The primary advantage was that the background irradiance was significantly lower, approximately half of the visible background irradiance. Another advantage was that the reflectance of these materials was approximately 10% higher in the infrared than the visible band. The main disadvantage of using the infrared spectrum was the absorption of many infrared bands due to water vapor in the atmosphere.

Figure 27 shows the results for an infrared flare between 1.1 and 1.4 microns, using a 5% BRDF at the observer's position. Similar to the visible flares, this infrared flare produced detectable SNR's, though the same caveat of applies.

By choosing the appropriate bandwidths the atmospheric transmittance can be optimized to over 95.8%. Such a window occurs between 1.639 and 1.650 microns. There are other infrared windows that would also work. The resulting narrowband flares are shown in Figure 28.

A narrowband comparison of the broad bandwidth infrared is shown in Figure 29. This shows that there is not a large difference in between the narrowband and broadband

cases. In this particular case, the broadband had a higher SNR than the narrowband flare. This would not always be true. The results could be skewed either way, depending on the particular IR wavelengths used and atmospheric attenuation characteristics.

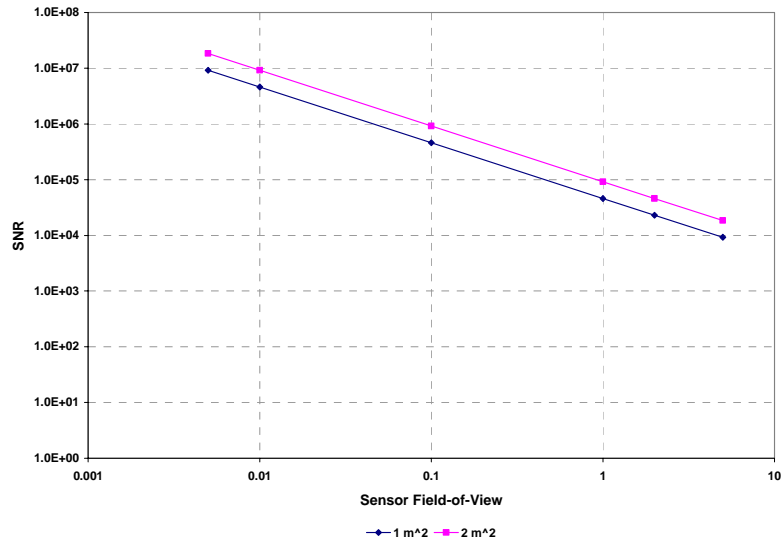


Figure 27. SNR for broadband infrared flare

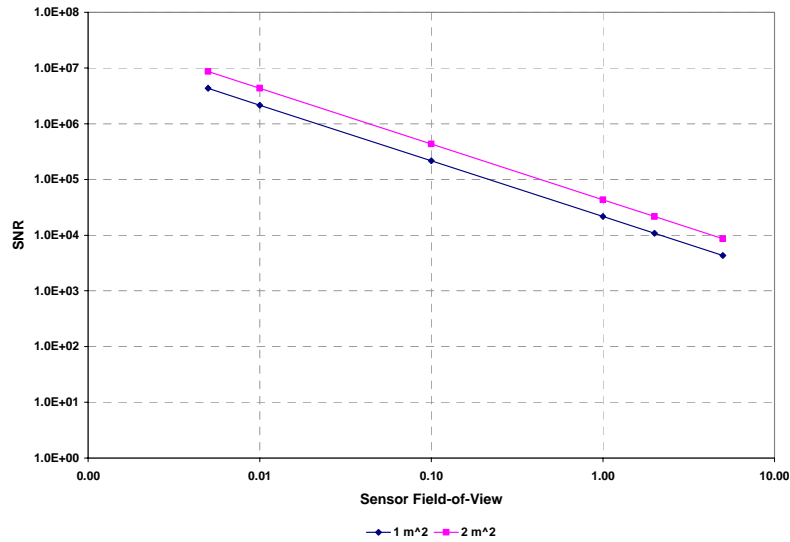


Figure 28. SNR for narrowband infrared flare

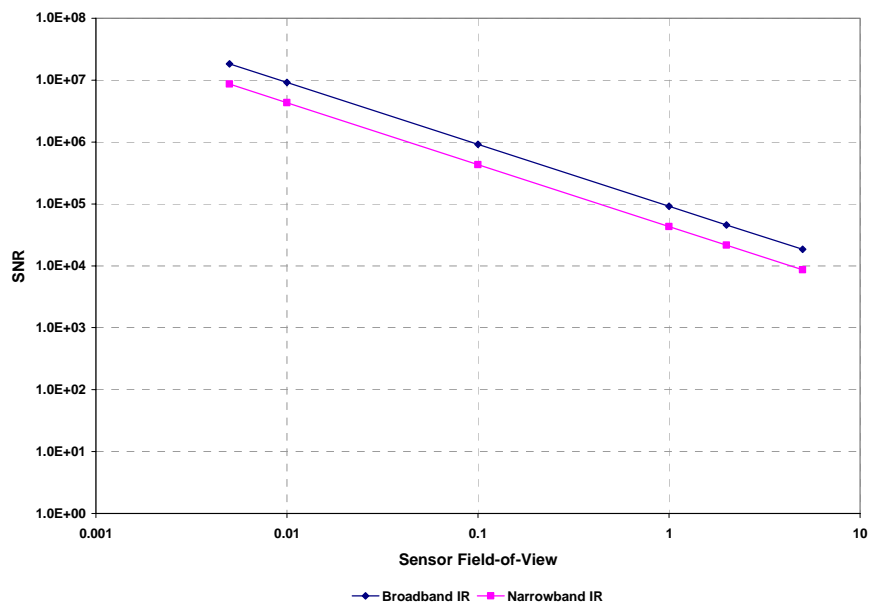


Figure 29. Comparison of narrowband and broadband infrared flares

4.2.5 Visible Versus Infrared Flares

Before comparing the visible and infrared results side-by-side, it proves useful to compare the atmospheric transmission of these two regions examined. Figure 30 shows the atmospheric transmittance windows from the visible through the near infrared. The lines at 0.4 and 0.7 microns show the approximate boundaries of the visible spectrum. Here, the spectrum has a more or less linear transmittance increasing from the violet up through the red. The lines at 1.15 and 1.35 microns show the window used with the infrared flare events described below. The infrared window has a number of transmission windows that are relatively clear to the infrared.

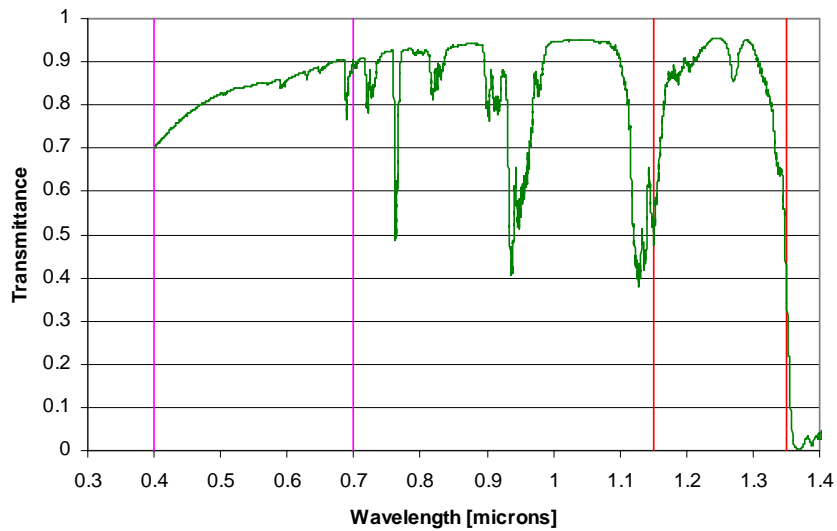


Figure 30. Visible and near IR atmospheric transmittance spectrum from PLEXUS

There are a number of infrared windows that could have been used for comparison with the visible results. The criterion used in selection was an infrared window that had higher transmittance while maintaining a roughly similar bandwidth to the visible bandwidth used. The average transmittance in the visible spectrum was approximately 0.82, whereas the chosen infrared region has an average transmittance of approximately 0.85.

The comparison of the visible and infrared flares is shown in Figure 31. The peak SNR's were $1.65e7$ and $1.09e7$ for the infrared and visible flares, respectively. There is a marginal improvement in SNR for the infrared flares. The particular attenuation window that the infrared flare lay in could affect the SNR of the infrared flare significantly.

Again, the SNR's of these visible and infrared flares should not be taken as an expected empirical result. These represent the best conditions. Real SNR's would be significantly lower.

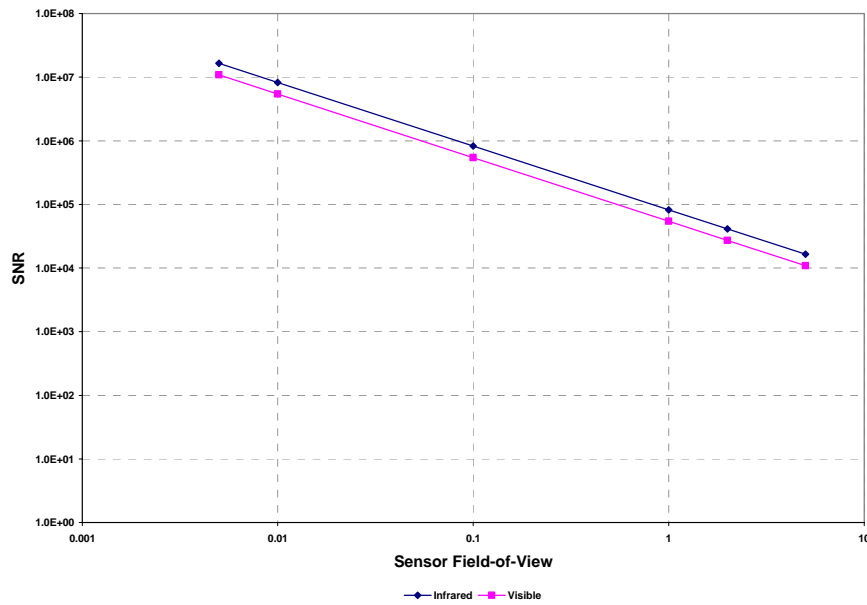


Figure 31. Comparison of SNR's for visible and infrared flares

4.3 Thermal Emissions

. The thermal characteristics of various space objects are presented in Table 7. The values for the SPOT 4 satellite are typical for most commercial satellites. The values for the nuclear reactor are from now vintage Soviet era nuclear reactor powered spacecraft. These were fairly rare, even in their day, but they represented a good object for comparison.

Table 7. Space object thermal characteristics³⁷

Temperature	Representative Object	Peak Wavelength [microns]	Spectral Band [microns]	Atmospheric Transmittance	Emission Source Size [m ²]
353 K	SPOT 4	8.21	8.05 – 8.51	0.73	2
900 K	Nuclear Reactor	3.22	3.1 – 3.71	0.57	20
1300 K	Reference	2.23	2.02 – 2.43	0.86	2

The SNR's of these objects are presented in Figure 32. In general, the hotter the

object, the larger the SNR. However, the 900 K nuclear reactor, had a larger SNR than the 1300 K object. This was due to the large emitting surface of on-board radiator on nuclear powered spacecraft. These spacecraft have far greater thermal control concerns than smaller, conventionally powered satellites, hence the larger radiator. As was seen with the flares, these objects produced detectable SNR's under idealized conditions

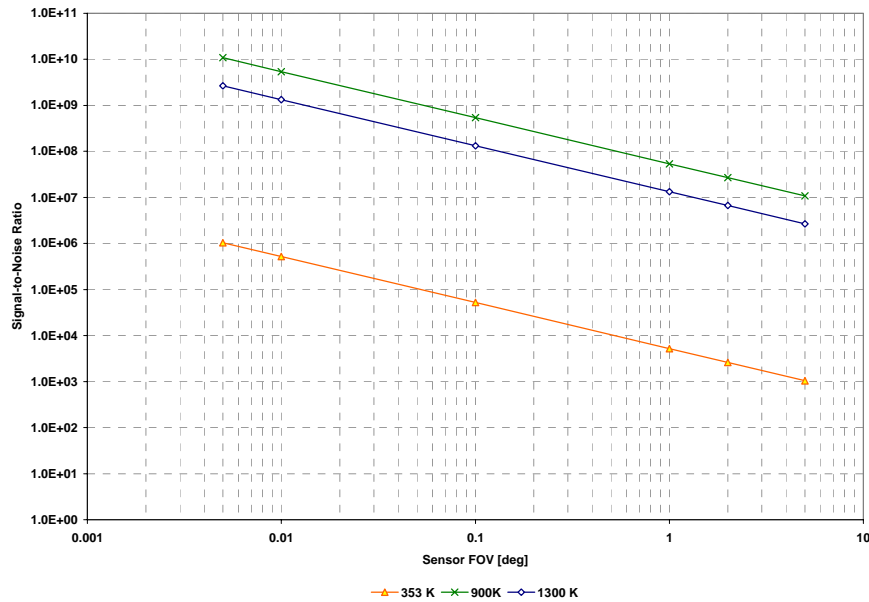


Figure 32. Signal-to-Noise Ratios for various space objects

4.4 Summary

With nighttime Iridium flares as a reference, daytime flares also produced detectable flare SNR's, though they were not as great as the nighttime flares. Infrared flares proved to be slightly more detectable than the visible flares, though this would not always be true, depending on the spectral transmission characteristics of the IR window.

Given that all space objects produce some thermal emissions, depending on temperature and emissivity, these results were more applicable to most orbiting objects.

While the SNR's were above the detectable level, it is not clear that this would always be the case, once other noises sources are introduced.

While the SNR was detectable for both the flares and the thermal emissions, the SBR is significantly below one. This makes it difficult to actually detect the signal since the background level would dominate the signal. Techniques exist that can still produce a detectable signal, even it is significantly below the background level. These techniques are briefly discussed in the next chapter.

V. Conclusions and Recommendations

5.1 Chapter Overview

This chapter reviews the results, draws conclusions, and makes recommendations for future work.

5.2 Conclusions of Research

A variety of factors can affect the visibility of these flares. A small projected area for the reflecting surface can greatly inhibit the received flare radiance. The observer's position relative to the center of the flare also plays a significant role. A few degrees off of the center, the BRDF drops to less than 1% of its peak. Finally, atmospheric attenuation and the spectral band observed can alter the flare intensity. Observing flares in the infrared improves the situation considerably, given a clear atmospheric spectral window.

The SNR's presented here represent the absolute best case scenarios. Real world SNR's will be considerably lower once other noise sources are introduced. The nighttime Iridium flares were easily detected. The daytime flares, while detectable, had significantly lower SNR's than the nighttime flares.

While the SNR's presented here were high, the SBR's were less than one. However, since the noise is constant, there is information about the target that should allow detection as evidence by large SNR's. How to do this was not addressed in this research, but is an area of future work.

For satellites other than Iridium satellites, there are a variety of hurdles that would make sun glints exceedingly difficult to detect. These hurdles include unknown

geometries, materials, attitude control, and orbit. Daylight tracking of space objects producing flares may prove more practical than attempting daytime detection.

Satellite thermal emissions are dependent on the temperature of the emitting surface of the satellite. Most satellites are relatively cool, except when solar illuminated. These objects were detectable, using carefully selected infrared spectral windows. Real world sensors, have fixed performance characteristics, and can not be arbitrarily adjusted to the optimized conditions presented here.

Thus, while the simulated flares and thermal emissions presented here did show detectable SNR's, the results need to be expanded upon with more numerous and realistic scenarios.

5.3 Significance of Research

This research was a necessary step towards proving whether daytime space object detection is possible with optical sensors. This was only a first step and techniques may improve upon these building blocks. Adding the ability to detect some space objects during the daytime will increase the utilization rates of the sensors of the Space Surveillance Network. This would improve Space Situational Awareness, protecting U.S. assets in space and on the ground.

5.4 Recommendations for Future Research

I have several recommendations for future research. First among them is to validate this model. Given that real-world conditions are not as pristine as some of the assumptions used in this thesis, many more simulations will need to be accomplished for comparison with empirical data.

There are a number of imaging techniques used to detect objects that lie below the background level. These techniques usually involve longer integration periods than is typical for Earth orbiting objects, but the principles are similar and may be applicable. Image stacking and tilt/nod techniques also exist that can produce images of objects that lie far below the background signal.³⁸ These techniques should be evaluated for applicability to this model and applied as appropriate to improve the capabilities of this model.

Studies of the variations in the reflected sunlight may prove useful to providing knowledge about the rotation rate or crude geometry of the object. Day-night terminator observations may provide a baseline for geometric techniques in tracking and detection. Other methods can be used to improve object knowledge and further improve the baseline for optical observations.

Other methods of object lighting should be considered for different observation periods. Reflected sunlight due to the Earth's albedo may impact object illumination. Moonlight illumination should also be considered when imaging space objects.

Spectral windows were chosen somewhat arbitrarily. These should be refined to accommodate existing or near-term sensors. Some analysis could be conducted in the ultraviolet regime using solar-blind detectors to determine if this is a viable option.

Narrowband and polarizing filters should be carefully looked at in order to determine their utility in expanding this model. It is speculated that polarizing filters may significantly boost the capabilities of detecting reflected light.

In order to speed the data manipulation, a consolidating set of software packages

and data manipulation algorithms need to be developed. A good deal of the time spent in developing this thesis was spent manipulating the vast quantities of data by hand.

The effect of the solar flare angle and slant range needs to be looked at further. It seems that there may be some optimal sun-Satellite positions to detect the satellite. Along these lines, exclusion zones around the sun need to be evaluated to develop filters that exclude certain geometries as very unlikely for detection to occur.

A small FOV decreases the background signal, improving detectability, yet effectively reduces the search window to that of looking through a soda straw. Thus, actual detection of a satellite would be extremely difficult. A balance must be struck between the size of the FOV and the amount of acceptable background noise. Analysis of this balance should lead to a better set up ground rules for sensor selection.

5.5 Summary

After a number of hurdles, it appears that daytime detection may be possible under some conditions. Detection may well have limited utility, given all the difficulties involved. Daytime tracking, however, may be a more practical application of this thesis. Further analysis and model validation needs to be accomplished, however.

VI. Appendix

1. Matlab® Iridium Satellite Model Source Code

```
function iridium_angles
% generates Iridium satellite model and rotates around model
% Inputs: Site azimuth and elevation, Sun azimuth and Elevation from satellite
% Alistair Funge, Capt USAF
% Air Force Institute of Technology, Applied Physics
% based on code developed by Capt Ruben Martinez

clear all;
close all;
clc;

format compact;

iridium_model1          % build satellite model -
% 7 panels X1-X7, Y, Z

az = input('Enter site azimuth from satellite {0..360}: ');
if isempty(az)
    az = 185.51; % default
end

al = input('Enter site altitude from satellite {0..360}: ');
if isempty(al)
    al = -44; % default
end

MMA = input('Enter MMA of interest {F, L, R} [R]: ','s');
if isempty(MMA)
    MMA = 'R'; % default
end

str(1) = {'Site Azimuth = ',num2str(az),' [deg]'};
str(2) = {'Site altitude = ',num2str(al),' [deg]'};

lightAz = input('Enter sun azimuth from satellite: ');
if isempty(lightAz)
    lightAz = 76.89; % default
end
```



```

lightAl = input('Enter sun altitude/Altitude from satellite: ');
if isempty(lightAl)
    lightAl = -7.96; % default
end

str(3) = {'sun Azimuth = ',num2str(lightAz),' [deg]'};
str(4) = {'sun altitude= ',num2str(lightAl),' [deg]'};

for Loop = 1:7 % 1:7 for all panels

    switch Loop
        case 1
            [Xnp,Ynp,Znp,area(Loop)] = Normalsp(X1,Y1,Z1);
        case 2
            [Xnp,Ynp,Znp,area(Loop)] = Normalsp(X2,Y2,Z2);
        case 3
            [Xnp,Ynp,Znp,area(Loop)] = Normalsp(X3,Y3,Z3);
        case 4
            [Xnp,Ynp,Znp,area(Loop)] = Normalsp(X4,Y4,Z4);
        case 5
            [Xnp,Ynp,Znp,area(Loop)] = Normalsp(X5,Y5,Z5);
        case 6
            [Xnp,Ynp,Znp,area(Loop)] = Normalsp(X6,Y6,Z6);
        otherwise
            [Xnp,Ynp,Znp,area(Loop)] = Normalsp(X7,Y7,Z7);
    end % switch

    reso=size(X1); % Resolution is size of coordinates
    res=reso(2);
    % A vector components from Normal
    Ax=Xnp(:,1)-Xnp(:,2);
    Ay=Ynp(:,1)-Ynp(:,2);
    Az=Znp(:,1)-Znp(:,2);

    [magA,magB,AdotB]=dotprod(az,al,Ax,Ay,Az);

    % Finds the angle between observer and Normal
    psi(Loop) = 180/pi*acos(AdotB./(magA*magB));
    % If >90, then not in FOV
    mask=psi(Loop)<89.99;
    % Cosine of the angle for projected area
    projector(Loop) = cos(pi/180*psi(Loop)).*mask;
    parea(Loop) = area(Loop)*projector(Loop);

```

```

str(Loop+4) = {'Panel ',num2str(Loop), ' projected area = ', num2str(parea(Loop)),...
    ' [cm^2]'};

plotSizeX = 2;
plotSizeY = 3;
loop=1

fig1=figure(loop);
set(gcf,'Units','normalized','Position',[.2 .2 .3 .65]);

colormap([0.9 0.9 0.9]);

subplot(3, 2,[1 2 3 4]);
surf(X1,Y1,Z1,'DisplayName','Front Panel');
hold on;

subplot(3, 2,[1 2 3 4]);
surf(X2,Y2,Z2,'DisplayName','Left Panel'); % panel 2
subplot(3, 2,[1 2 3 4]);
surf(X3,Y3,Z3,'DisplayName','Right Panel');

switch MMA % color MMA of interest in Red [1 0 0]
case {'F' 'f'}
    FrontMMAColor = [1 0 0];
    LeftMMAColor = [0.9 0.9 0.9];
    RightMMAColor = [0.9 0.9 0.9];
case {'L' 'l'}
    FrontMMAColor = [0.9 0.9 0.9];
    LeftMMAColor = [1 0 0];
    RightMMAColor = [0.9 0.9 0.9];
otherwise % MMA = R or r
    FrontMMAColor = [0.9 0.9 0.9];
    LeftMMAColor = [0.9 0.9 0.9];
    RightMMAColor = [1 0 0];
end

subplot(3, 2,[1 2 3 4]);
surf(X4,Y4,Z4,'DisplayName','Front MMA','FaceColor', FrontMMAColor);
subplot(3, 2,[1 2 3 4]);
surf(X5,Y5,Z5,'DisplayName','Left MMA','FaceColor', LeftMMAColor);
subplot(3, 2,[1 2 3 4]);
surf(X6,Y6,Z6,'DisplayName','Right MMA','FaceColor', RightMMAColor);

```

```

subplot(3, 2,[1 2 3 4]);
surf(X7,Y7,Z7,'DisplayName','Base');
subplot(3, 2,[1 2 3 4]);
line([62.5 62.5],[0 -250],[199 199],'LineWidth',2,'Marker','+');

xlabel('x [cm]');
ylabel('y [cm]');
zlabel('z [cm]');
title('\bfIridium Satellite Model\rm');
axis equal;

camtarget([62.5 62.5 199]);
view(az, al);

if loop == 1
    annotation1 = annotation(...
        fig1,'textbox',...
        'Position',[0.15 0.05 0.45 0.3],...
        'String',str,...
        'FitHeightToText','on',...
        'BackgroundColor',[1 1 1]);
end

light('style','infinite');
light_handle = lightangle(lightAz,lightAl);

figure;

for azloop = az-180:az+180
    view(azloop,al);
    pause(.01);
end

plotSizey=2;
plotSizex=2;

end %for loop = 1:2

return; % function

% %*****

function [magA,magB,AdotB]=dotprod(az,al,Ax,Ay,Az)
% Since centerline on x-y plane

```

```

theta=(al+90)*pi/180;    % For nose-on aspect
phi=(az+90)*pi/180;     % X,Y,Z converted from spherical coordinate system
x=sin(theta)*cos(phi);  % This is where the observer is at. R = 1 to make
y=sin(theta)*sin(phi);  % observer vector a unit vector
z=cos(theta)*ones(size(y));

```

```

Bx=x;                    % B vector components

```

```

By=y;

```

```

Bz=z;

```

```

% Definition of dot product

```

```

AdotB=Ax*Bx+Ay*By+Az*Bz;

```

```

% Magnitude of each vector

```

```

magA=sqrt(Ax.^2+Ay.^2+Az.^2);

```

```

magB=sqrt(Bx.^2+By.^2+Bz.^2);

```

```

return;

```

```

function iridium_model1

```

```

% Capt Alistair Funge

```

```

[aX aY aZ]=Trap(188,86,0,86,2); % antenna trapazoid

```

```

[bX bY bZ]=Trap(398,125,0,125,2); % body panel trapazoid

```

```

[cX cY cZ]=Trap(108.3,125,62.5,62.5,2); % triangle for base

```

```

% body panel 1

```

```

psi=0; chi=0; phi=90;

```

```

Lx=0; Ly=0; Lz=0;

```

```

[X1 Y1 Z1]=EulerAngles(psi,chi,phi,Lx,Ly,Lz,bX,bY,bZ);

```

```

% antenna 1

```

```

psi=0; chi=0; phi=130;

```

```

Lx=19.5; Ly=0; Lz=80;

```

```

[X4 Y4 Z4]=EulerAngles(psi,chi,phi,Lx,Ly,Lz,aX,aY,aZ);

```

```

% body panel 2

```

```

psi=240; chi=0; phi=90; %y, z, x

```

```

Lx=62.5; Ly=108.3; Lz=0;

```

```

[X2 Y2 Z2]=EulerAngles(psi,chi,phi,Lx,Ly,Lz,bX,bY,bZ);

```

```

% antenna 2

```

```

psi=180; chi=0; phi=50;

```

```

Lx=0; Ly=0; Lz=0;

```

```

[X5 Y5 Z5]=EulerAngles(psi,chi,phi,Lx,Ly,Lz,aX,aY,aZ);

```

```

psi=0; chi=60; phi=0;

```

```

[X5 Y5 Z5]=EulerAngles(psi,chi,phi,Lx,Ly,Lz,X5,Y5,Z5);

```

```

psi=0; chi=0; phi=0;
Lx=52.75; Ly=91.4; Lz=80;
[X5 Y5 Z5]=EulerAngles(psi,chi,phi,Lx,Ly,Lz,X5,Y5,Z5);

% body panel 3
psi=120; chi=0; phi=90;
Lx=125; Ly=0; Lz=0;
[X3 Y3 Z3]=EulerAngles(psi,chi,phi,Lx,Ly,Lz,bX,bY,bZ);

% antenna 3
psi=0; chi=0; phi=130;
Lx=0; Ly=0; Lz=0;
[X6 Y6 Z6]=EulerAngles(psi,chi,phi,Lx,Ly,Lz,aX,aY,aZ);
psi=0; chi=120; phi=0;
[X6 Y6 Z6]=EulerAngles(psi,chi,phi,Lx,Ly,Lz,X6,Y6,Z6);
psi=0; chi=0; phi=0;
Lx=115.25; Ly=16.89; Lz=80;
[X6 Y6 Z6]=EulerAngles(psi,chi,phi,Lx,Ly,Lz,X6,Y6,Z6);

% triangle base
psi=0; chi=180; phi=180;
Lx=125; Ly=0; Lz=0;
[X7 Y7 Z7]=EulerAngles(psi,chi,phi,Lx,Ly,Lz,cX,cY,cZ);

psi=0; chi=0; phi=0;
Lx=125; Ly=0; Lz=0;
[X8 Y8 Z8]=EulerAngles(psi,chi,phi,Lx,Ly,Lz,-50,50,0);

return;

function [XT,YT,ZT]=Trap(height,baselength,topstart,topend,reso)
% [XT,YT,ZT]=Trap(height,baselength,topstart,topend,reso)
%
% Ruben Martinez, 4 Oct 04
% Function that creates a trapezoid where 'height' is the
% height of the trapezoid, 'baselength' is the length
% trapezoid's base. Starting point is always (0,0) - use
% function 'EulerAngles' to translate or rotate.
% 'topstart' is the starting x-coordinate for the top of the
% trapezoid, 'topend' is the ending x-coordinate for the
% top of the trapezoid. 'reso' is the resolution.
% If no argument for 'reso' is entered, the resolution
% is defaulted to 10.
%

```

```

% Example: Trap(8,8,7,9)
% produces: (7,8) (9,8)
%           x----x
%          /  /
%         /  /
%        /  /
%       x-----x
%      (0,0) (8,0)
%
% Can also produce squares or rectangles...

if nargin==5
    res=reso;
else
    res=10;
end

zt=0;
ml=height/(topstart);      % Slope of left line
mr=height/(topend-baslength); % Slope of right line
b=-mr*baslength;          % y-intercept for right line
                           % y-intercept for left line is 0
yh=linspace(0,height,res);
for n=1:length(yh)
    if topstart==0
        xs=topstart;      % To create straight line
    else
        xs=yh(n)./ml;      % Solve for left x-coord for given y
    end;
    if (topend-baslength)==0
        xe=topend;        % To create straight line
    else
        xe=(yh(n)-b)./mr;  % Solve for right x-coord for given y
    end
    XT(n,:)=linspace(xs,xe,length(yh)); % Create x-vector for given y
    YT(n,:)=linspace(yh(n),yh(n),length(yh)); % Create y-vector
    ZT(n,:)=linspace(0,zt,length(yh));   % Create z-vector
end

function [nX,nY,nZ,pareas] = Normalsp(Xp,Yp,Zp)
% [nX,nY,nZ,pareas] = Normalsp(Xp,Yp,Zp)
%
% Ruben Martinez, 15 Oct 04
% Calculates the normals to the center of

```

```

% each patch.
% Also computes the area of each patch

mat=size(Xp);      % To find number of rows and columns
count=0;
for n=1:mat(1)-1   % Rows
    for m=1:mat(2)-1 % Columns
        count=count+1;

        % If triangular facet
        if Xp(n,m)==Xp(n,m+1) & Yp(n,m)==Yp(n,m+1)...
            & Zp(n,m)==Zp(n,m+1)
            % X-Components
            Ax=Xp(n,m)-Xp(n+1,m);
            Bx=Xp(n+1,m+1)-Xp(n+1,m);

            % Y-Components
            Ay=Yp(n,m)-Yp(n+1,m);
            By=Yp(n+1,m+1)-Yp(n+1,m);

            % Z-Components
            Az=Zp(n,m)-Zp(n+1,m);
            Bz=Zp(n+1,m+1)-Zp(n+1,m);

            % Cross Products
            % A cross B
            ABx=(Ay*Bz-Az*By);
            ABY=(Az*Bx-Ax*Bz);
            ABz=(Ax*By-Ay*Bx);

            % Area of Patch
            pareas(count,1)=0.5*(sqrt(ABx^2+ABY^2+ABz^2));

            % Midpoint of E
            Ex1=0.5*(Xp(n+1,m+1)+Xp(n+1,m));
            Ey1=0.5*(Yp(n+1,m+1)+Yp(n+1,m));
            Ez1=0.5*(Zp(n+1,m+1)+Zp(n+1,m));
            Ex=0.5*(Xp(n,m)+Ex1);
            Ey=0.5*(Yp(n,m)+Ey1);
            Ez=0.5*(Zp(n,m)+Ez1);

            % Normal from A cross B
            nx=(ABx/sqrt(ABx^2+ABY^2+ABz^2))+Ex;
            ny=(ABY/sqrt(ABx^2+ABY^2+ABz^2))+Ey;

```

```

nz=(ABz/sqrt(ABx^2+ABy^2+ABz^2))+Ez;

% Normal Coordinates for Plotting
nXp(2*count-1,:)= [Ex nx];
nYp(2*count-1,:)= [Ey ny];
nZp(2*count-1,:)= [Ez nz];
nXp(2*count,:)= [NaN NaN];
nYp(2*count,:)= [NaN NaN];
nZp(2*count,:)= [NaN NaN];

% Normal Coordinates
nX(count,:)= [Ex nx];
nY(count,:)= [Ey ny];
nZ(count,:)= [Ez nz];

%%%%%%%%%%%% If triangular facet
elseif Xp(n,m)==Xp(n+1,m) & Yp(n,m)==Yp(n+1,m) ...
    & Zp(n,m)==Zp(n+1,m)
% X-Components
Ax=Xp(n,m+1)-Xp(n,m);
Bx=Xp(n+1,m+1)-Xp(n,m);

% Y-Components
Ay=Yp(n,m+1)-Yp(n,m);
By=Yp(n+1,m+1)-Yp(n,m);

% Z-Components
Az=Zp(n,m+1)-Zp(n,m);
Bz=Zp(n+1,m+1)-Zp(n,m);

% Cross Products
% A cross B
ABx=(Ay*Bz-Az*By);
ABy=(Az*Bx-Ax*Bz);
ABz=(Ax*By-Ay*Bx);

% Area of Patch
pareas(count,1)=0.5*(sqrt(ABx^2+ABy^2+ABz^2));

% Midpoint of E
Ex1=0.5*(Xp(n,m+1)+Xp(n+1,m+1));
Ey1=0.5*(Yp(n,m+1)+Yp(n+1,m+1));
Ez1=0.5*(Zp(n,m+1)+Zp(n+1,m+1));
Ex=0.5*(Xp(n,m)+Ex1);

```



```

Ey=0.5*(Yp(n,m)+Ey1);
Ez=0.5*(Zp(n,m)+Ez1);

% Normal from A cross B
nx=(ABx/sqrt(ABx^2+ABy^2+ABz^2))+Ex;
ny=(ABy/sqrt(ABx^2+ABy^2+ABz^2))+Ey;
nz=(ABz/sqrt(ABx^2+ABy^2+ABz^2))+Ez;

% Normal Coordinates for Plotting
nXp(2*count-1,:)= [Ex nx];
nYp(2*count-1,:)= [Ey ny];
nZp(2*count-1,:)= [Ez nz];
nXp(2*count,:)= [NaN NaN];
nYp(2*count,:)= [NaN NaN];
nZp(2*count,:)= [NaN NaN];

% Normal Coordinates
nX(count,:)= [Ex nx];
nY(count,:)= [Ey ny];
nZ(count,:)= [Ez nz];

%%%%%%%%%%%% If triangular facet
elseif Xp(n,m+1)==Xp(n+1,m+1) & Yp(n,m+1)==Yp(n+1,m+1)...
    & Zp(n,m+1)==Zp(n+1,m+1)
% X-Components
Ax=Xp(n+1,m+1)-Xp(n,m);
Bx=Xp(n+1,m)-Xp(n,m);

% Y-Components
Ay=Yp(n+1,m+1)-Yp(n,m);
By=Yp(n+1,m)-Yp(n,m);

% Z-Components
Az=Zp(n+1,m+1)-Zp(n,m);
Bz=Zp(n+1,m)-Zp(n,m);

% Cross Products
% A cross B
ABx=(Ay*Bz-Az*By);
ABy=(Az*Bx-Ax*Bz);
ABz=(Ax*By-Ay*Bx);

% Area of Patch
pareas(count,1)=0.5*(sqrt(ABx^2+ABy^2+ABz^2));

```

```

% Midpoint of E
Ex1=0.5*(Xp(n+1,m)+Xp(n,m));
Ey1=0.5*(Yp(n+1,m)+Yp(n,m));
Ez1=0.5*(Zp(n+1,m)+Zp(n,m));
Ex=0.5*(Xp(n+1,m+1)+Ex1);
Ey=0.5*(Yp(n+1,m+1)+Ey1);
Ez=0.5*(Zp(n+1,m+1)+Ez1);

% Normal from A cross B
nx=(ABx/sqrt(ABx^2+ABy^2+ABz^2))+Ex;
ny=(ABy/sqrt(ABx^2+ABy^2+ABz^2))+Ey;
nz=(ABz/sqrt(ABx^2+ABy^2+ABz^2))+Ez;

% Normal Coordinates for Plotting
nXp(2*count-1,:)= [Ex nx];
nYp(2*count-1,:)= [Ey ny];
nZp(2*count-1,:)= [Ez nz];
nXp(2*count,:)= [NaN NaN];
nYp(2*count,:)= [NaN NaN];
nZp(2*count,:)= [NaN NaN];

% Normal Coordinates
nX(count,:)= [Ex nx];
nY(count,:)= [Ey ny];
nZ(count,:)= [Ez nz];

%%%%%%%%%%%% If triangular facet
elseif Xp(n+1,m+1)==Xp(n+1,m) & Yp(n+1,m+1)==Yp(n+1,m)...
    & Yp(n+1,m+1)==Yp(n+1,m)
% X-Components
Ax=Xp(n,m+1)-Xp(n,m);
Bx=Xp(n+1,m+1)-Xp(n,m);

% Y-Components
Ay=Yp(n,m+1)-Yp(n,m);
By=Yp(n+1,m+1)-Yp(n,m);

% Z-Components
Az=Zp(n,m+1)-Zp(n,m);
Bz=Zp(n+1,m+1)-Zp(n,m);

% Cross Products
% A cross B

```

```

ABx=(Ay*Bz-Az*By);
ABy=(Az*Bx-Ax*Bz);
ABz=(Ax*By-Ay*Bx);

% Area of Patch
pareas(count,1)=0.5*(sqrt(ABx^2+ABy^2+ABz^2));

% Midpoint of E
Ex1=0.5*(Xp(n+1,m+1)+Xp(n,m));
Ey1=0.5*(Yp(n+1,m+1)+Yp(n,m));
Ez1=0.5*(Zp(n+1,m+1)+Zp(n,m));
Ex=0.5*(Xp(n,m+1)+Ex1);
Ey=0.5*(Yp(n,m+1)+Ey1);
Ez=0.5*(Zp(n,m+1)+Ez1);

% Normal from A cross B
nx=(ABx/sqrt(ABx^2+ABy^2+ABz^2))+Ex;
ny=(ABy/sqrt(ABx^2+ABy^2+ABz^2))+Ey;
nz=(ABz/sqrt(ABx^2+ABy^2+ABz^2))+Ez;

% Normal Coordinates for Plotting
nXp(2*count-1,:)= [Ex nx];
nYp(2*count-1,:)= [Ey ny];
nZp(2*count-1,:)= [Ez nz];
nXp(2*count,:)= [NaN NaN];
nYp(2*count,:)= [NaN NaN];
nZp(2*count,:)= [NaN NaN];

% Normal Coordinates
nX(count,:)= [Ex nx];
nY(count,:)= [Ey ny];
nZ(count,:)= [Ez nz];

%%%%%%%%%%%% If quadrilateral
else
% X-Components
Ax=Xp(n+1,m)-Xp(n,m);
Bx=Xp(n,m+1)-Xp(n,m);
Cx=Xp(n+1,m)-Xp(n+1,m+1);
Dx=Xp(n,m+1)-Xp(n+1,m+1);

% Y-Components
Ay=Yp(n+1,m)-Yp(n,m);
By=Yp(n,m+1)-Yp(n,m);

```

```

Cy=Yp(n+1,m)-Yp(n+1,m+1);
Dy=Yp(n,m+1)-Yp(n+1,m+1);

% Z-Components
Az=Zp(n+1,m)-Zp(n,m);
Bz=Zp(n,m+1)-Zp(n,m);
Cz=Zp(n+1,m)-Zp(n+1,m+1);
Dz=Zp(n,m+1)-Zp(n+1,m+1);

% Cross Products
% A cross B
ABx=-(Ay*Bz-Az*By);
ABy=-(Az*Bx-Ax*Bz);
ABz=-(Ax*By-Ay*Bx);
% D cross C
DCx=Dy*Cz-Dz*Cy;
DCy=Dz*Cx-Dx*Cz;
DCz=Dx*Cy-Dy*Cx;

% Area of Patch
areas(count,1)=0.5*(sqrt(ABx^2+ABy^2+ABz^2))+...
    0.5*(sqrt(DCx^2+DCy^2+DCz^2));

% Midpoint of E
Ex=0.5*(Xp(n+1,m+1)+Xp(n,m));
Ey=0.5*(Yp(n+1,m+1)+Yp(n,m));
Ez=0.5*(Zp(n+1,m+1)+Zp(n,m));

% Normal from A cross B
nx=(ABx/sqrt(ABx^2+ABy^2+ABz^2))+Ex;
ny=(ABy/sqrt(ABx^2+ABy^2+ABz^2))+Ey;
nz=(ABz/sqrt(ABx^2+ABy^2+ABz^2))+Ez;

% Normal Coordinates for Plotting
nXp(2*count-1,:)= [Ex nx];
nYp(2*count-1,:)= [Ey ny];
nZp(2*count-1,:)= [Ez nz];
nXp(2*count,:)= [NaN NaN];
nYp(2*count,:)= [NaN NaN];
nZp(2*count,:)= [NaN NaN];

% Normal Coordinates
nX(count,:)= [Ex nx];
nY(count,:)= [Ey ny];

```

```
    nZ(count,:)=[Ez nz];  
end  
end  
end
```

```
if nargout==0  
    surf(Xp,Yp,Zp);  
    hold on;  
    surf(nXp,nYp,nZp);  
end
```

2. Iridium Two Line Element (TLE) Set ³⁹

IRIDIUM 8

1 24792U 97020A 04313.35171100 .00000046 00000-0 92795-5 0 5657
2 24792 86.3916 82.6709 0002303 77.9697 282.1788 14.34217290393323

IRIDIUM 7

1 24793U 97020B 04313.41513419 .00000085 00000-0 23161-4 0 5583
2 24793 86.3924 82.7085 0002263 79.2974 280.8500 14.34218029393338

IRIDIUM 6

1 24794U 97020C 04312.92041298 -.00000071 00000-0 -32503-4 0 3462
2 24794 86.3921 82.9252 0001612 97.5446 262.5931 14.34216437393266

IRIDIUM 5

1 24795U 97020D 04313.47222097 .00000237 00000-0 77472-4 0 6337
2 24795 86.3930 82.7983 0002249 80.5543 279.5954 14.34217522393420

IRIDIUM 4

1 24796U 97020E 04313.35805334 .00000263 00000-0 86778-4 0 5782
2 24796 86.3914 82.6186 0002178 80.9976 279.1483 14.34218528393343

IRIDIUM 914

1 24836U 97030A 04312.80478473 .00000235 00000-0 72391-4 0 8921
2 24836 86.3895 111.2768 0003891 78.6975 281.4662 14.37144261387362

IRIDIUM 12

1 24837U 97030B 04313.41855913 .00000167 00000-0 52546-4 0 5705
2 24837 86.3904 114.1991 0002299 75.0748 285.0724 14.34217214387088

IRIDIUM 10

1 24839U 97030D 04313.40587430 .00000136 00000-0 41411-4 0 5471
2 24839 86.3903 114.2087 0002325 73.8627 286.2843 14.34217019387097

IRIDIUM 13

1 24840U 97030E 04313.42490140 .00000094 00000-0 26638-4 0 5394
2 24840 86.3902 114.2385 0002178 73.5009 286.6457 14.34217138387082

IRIDIUM 16

1 24841U 97030F 04313.36781934 -.00000113 00000-0 -47296-4 0 5658
2 24841 86.3910 114.3847 0002254 75.9332 284.2118 14.34215208387079

IRIDIUM 911

1 24842U 97030G 04313.02024210 .00000757 00000-0 22104-3 0 9655
2 24842 86.4408 117.3170 0013103 221.9498 138.0714 14.42778503388706

IRIDIUM 15

1 24869U 97034A 04313.48540807 .00000118 00000-0 35206-4 0 5692
2 24869 86.3937 145.7969 0002344 77.5714 282.5759 14.34217301384067

IRIDIUM 17

1 24870U 97034B 04313.47906394 .00000124 00000-0 37218-4 0 5579
2 24870 86.3935 145.8206 0002326 79.3209 280.8255 14.34217769384061

IRIDIUM 920

1 24871U 97034C 04313.05958741 .00000136 00000-0 38508-4 0 9072
2 24871 86.3946 143.0278 0011619 351.5789 8.5256 14.37740482384507

IRIDIUM 18

1 24872U 97034D 04313.51711885 .00000041 00000-0 75894-5 0 5598
2 24872 86.3938 145.8625 0001183 97.1891 262.9469 14.34216748384060

IRIDIUM 921

1 24873U 97034E 04312.83154732 .00002109 00000-0 18857-3 0 1378
2 24873 86.3890 49.2304 0011248 113.9536 246.2873 14.95307916397619

IRIDIUM 26

1 24903U 97043A 04313.29412249 -.00000280 00000-0 -10707-3 0 6161
2 24903 86.3992 19.5360 0002332 83.9355 276.2106 14.34217192377975

IRIDIUM 25

1 24904U 97043B 04313.25606916 -.00000163 00000-0 -65153-4 0 5620
2 24904 86.3993 19.5289 0002327 85.0753 275.0718 14.34216091377935

IRIDIUM 46

1 24905U 97043C 04313.26875193 -.00000151 00000-0 -60885-4 0 5867
2 24905 86.3999 19.6525 0002368 85.7107 274.4314 14.34217263377949

IRIDIUM 23

1 24906U 97043D 04313.24338187 -.00000205 00000-0 -80286-4 0 5747
2 24906 86.3992 19.4978 0002335 83.1651 276.9792 14.34217005377944

IRIDIUM 22

1 24907U 97043E 04313.23703984 -.00000109 00000-0 -45925-4 0 5416
2 24907 86.4003 19.6691 0002346 85.5641 274.5818 14.34216721377947

DUMMY MASS 1

1 24925U 97048A 04312.80501564 .00000261 00000-0 28295-4 0 7750
2 24925 86.3379 2.8000 0009705 89.2110 271.0225 14.83602843388672

DUMMY MASS 2

1 24926U 97048B 04312.82830701 .00000195 00000-0 20356-4 0 7724
2 24926 86.3383 3.1752 0010470 92.3260 267.9152 14.83385706388622

IRIDIUM 29

1 24944U 97051A 04313.31657520 -.00000017 00000-0 -13256-4 0 5273
2 24944 86.3970 51.0986 0002251 82.9176 277.2278 14.34217030374521

IRIDIUM 32

1 24945U 97051B 04313.33560266 -.00000205 00000-0 -80146-4 0 5255
2 24945 86.3969 51.0960 0002252 83.6013 276.5438 14.34216252374548

IRIDIUM 33

1 24946U 97051C 04313.34194478 .00000253 00000-0 83259-4 0 4961
2 24946 86.3969 51.1042 0002260 83.9293 276.2180 14.34217829374534

IRIDIUM 28

1 24948U 97051E 04313.38000330 .00000238 00000-0 77981-4 0 3271
2 24948 86.3985 51.0835 0002217 81.5821 278.5680 14.34217306374525

IRIDIUM 30

1 24949U 97051F 04313.32925927 .00000013 00000-0 -25848-5 0 5511
2 24949 86.3967 51.1281 0002207 83.3524 276.7917 14.34217098374522

IRIDIUM 31

1 24950U 97051G 04313.32291639 .00000018 00000-0 -54119-6 0 5484
2 24950 86.3972 51.1077 0002213 82.8612 277.2827 14.34217247374535

IRIDIUM 19

1 24965U 97056A 04313.30731293 .00000163 00000-0 51173-4 0 5360
2 24965 86.3920 82.6507 0002299 80.0881 280.0591 14.34217029372674

IRIDIUM 35

1 24966U 97056B 04313.31999804 -.00000069 00000-0 -31678-4 0 5765
2 24966 86.3921 82.6824 0002262 80.3066 279.8408 14.34216582372650

IRIDIUM 36

1 24967U 97056C 04313.39610858 .00000119 00000-0 35258-4 0 5226
2 24967 86.3922 82.6744 0002280 78.9566 281.1923 14.34217872372809

IRIDIUM 37

1 24968U 97056D 04313.43416369 -.00000003 00000-0 -82900-5 0 5527
2 24968 86.3920 82.6797 0002258 81.5409 278.6044 14.34217117372679

IRIDIUM 34

1 24969U 97056E 04313.31365618 .00000143 00000-0 43910-4 0 5367
2 24969 86.3922 82.6927 0002294 78.7409 281.4064 14.34217457372654

IRIDIUM 43

1 25039U 97069A 04313.51077556 .00000054 00000-0 12125-4 0 5177
2 25039 86.3938 145.8759 0002267 80.5707 279.5771 14.34217623366467

IRIDIUM 41

1 25040U 97069B 04313.50443601 .00000049 00000-0 10321-4 0 5299
2 25040 86.3942 145.8349 0002297 80.6065 279.5392 14.34216819366465

IRIDIUM 40

1 25041U 97069C 04313.52980549 .00000118 00000-0 35029-4 0 5030
2 25041 86.3933 145.8126 0002333 79.2067 280.9413 14.34218003366485

IRIDIUM 39

1 25042U 97069D 04313.53614846 .00000120 00000-0 35610-4 0 5169
2 25042 86.3930 145.7991 0002319 79.6600 280.4877 14.34217685366465

IRIDIUM 38

1 25043U 97069E 04313.46403519 .00000154 00000-0 47819-4 0 5627
2 25043 86.3931 145.7115 0002288 83.3135 276.8330 14.34398125366502

IRIDIUM 42

1 25077U 97077A 04313.45369514 .00000010 00000-0 -35906-5 0 5423
2 25077 86.3933 145.8870 0002372 81.4598 278.6869 14.34216879362313

IRIDIUM 44

1 25078U 97077B 04313.03763016 -.00000181 00000-0 -68650-4 0 7897
2 25078 86.3946 144.1613 0001903 147.5325 212.6022 14.36296597362457

IRIDIUM 45

1 25104U 97082A 04313.26241141 -.00000055 00000-0 -26779-4 0 4611
2 25104 86.3987 19.5994 0002293 85.4560 274.6893 14.34216462360489

IRIDIUM 24

1 25105U 97082B 04312.69880017 .00000296 00000-0 91487-4 0 8526
2 25105 86.3964 15.6285 0012331 2.9194 357.2069 14.37887214360841

IRIDIUM 47

1 25106U 97082C 04313.27509565 .00000027 00000-0 24198-5 0 4803
2 25106 86.3984 19.5454 0002336 84.1356 276.0106 14.34216968360480

IRIDIUM 49

1 25108U 97082E 04313.28778051 -.00000365 00000-0 -13755-3 0 4873
2 25108 86.3993 19.5112 0002252 84.4046 275.7403 14.34216464360497

IRIDIUM 52

1 25169U 98010A 04313.45661470 .00000133 00000-0 40547-4 0 2708
2 25169 86.3905 114.2653 0002335 76.1230 284.0230 14.34217587351921

IRIDIUM 56

1 25170U 98010B 04313.38050340 .00000015 00000-0 -15755-5 0 2344
2 25170 86.3909 114.3028 0002233 81.8097 278.3363 14.34216788351896

IRIDIUM 54

1 25171U 98010C 04313.41221471 .00000242 00000-0 79446-4 0 4949
2 25171 86.3908 114.2808 0002302 75.5006 284.6462 14.34218200352069

IRIDIUM 50

1 25172U 98010D 04313.44392911 -.00000073 00000-0 -33170-4 0 4804
2 25172 86.3913 114.2459 0002256 78.0383 282.1086 14.34216698351908

IRIDIUM 53

1 25173U 98010E 04313.53272523 .00000022 00000-0 70291-6 0 4721
2 25173 86.3915 114.2183 0002281 80.9378 279.2085 14.34216858351925

IRIDIUM 51

1 25262U 98018A 04313.42336716 .00000281 00000-0 77703-4 0 5801
2 25262 86.4438 82.6372 0002307 83.3528 276.7944 14.43149994348845

IRIDIUM 61

1 25263U 98018B 04313.44050688 -.00000128 00000-0 -52752-4 0 4476
2 25263 86.3924 82.6706 0002261 85.6841 274.4592 14.34216355347005

IRIDIUM 55

1 25272U 98019A 04313.37365939 -.00000236 00000-0 -91316-4 0 4601
2 25272 86.3969 51.0300 0002283 84.9722 275.1733 14.34215896346191

IRIDIUM 57

1 25273U 98019B 04313.34828557 .00000176 00000-0 55828-4 0 4844
2 25273 86.3980 51.1463 0002237 88.2723 271.8772 14.34218518346193

IRIDIUM 58

1 25274U 98019C 04313.35462934 .00000089 00000-0 24834-4 0 2584
2 25274 86.3973 51.1976 0002236 83.8934 276.2477 14.34217673346191

IRIDIUM 59

1 25275U 98019D 04313.36097284 .00000046 00000-0 95394-5 0 2299
2 25275 86.3983 51.2238 0002425 58.2818 301.8612 14.34217428346196

IRIDIUM 60

1 25276U 98019E 04313.50685154 -.00000118 00000-0 -49087-4 0 5028
2 25276 86.3975 51.0382 0002256 87.2196 272.9267 14.34216572346215

IRIDIUM 62

1 25285U 98021A 04313.46829192 .00000043 00000-0 83727-5 0 4729
2 25285 86.3976 347.8870 0002349 88.8991 271.2476 14.34217373345164

IRIDIUM 63

1 25286U 98021B 04313.12579289 -.00000106 00000-0 -44803-4 0 4567
2 25286 86.3978 348.0766 0002369 86.2298 273.9161 14.34216681345114

IRIDIUM 64

1 25287U 98021C 04313.20190336 .00000050 00000-0 10823-4 0 4425
2 25287 86.3979 348.0140 0002373 88.0853 272.0614 14.34217171345101

IRIDIUM 65

1 25288U 98021D 04313.48732020 -.00000021 00000-0 -14537-4 0 4637
2 25288 86.3978 347.8703 0002377 86.4557 273.6911 14.34217018345163

IRIDIUM 66

1 25289U 98021E 04313.49366386 .00000011 00000-0 -31306-5 0 4639
2 25289 86.3975 347.8115 0002302 84.6214 275.5253 14.34216738345164

IRIDIUM 67

1 25290U 98021F 04313.15116211 -.00000135 00000-0 -55360-4 0 2400
2 25290 86.3973 348.0184 0002386 84.2622 275.8840 14.34217130345122

IRIDIUM 68

1 25291U 98021G 04313.22727310 -.00000268 00000-0 -10269-3 0 4617
2 25291 86.3976 348.0228 0002360 89.8950 270.2519 14.34216641345108

IRIDIUM 69

1 25319U 98026A 04313.23800683 .00000217 00000-0 67048-4 0 3179
2 25319 86.4010 18.6248 0000757 131.0650 229.0619 14.36742335341640

IRIDIUM 71

1 25320U 98026B 04312.72779298 .00000277 00000-0 86182-4 0 7777
2 25320 86.4013 17.2336 0003116 31.1315 329.0065 14.37352954341751

IRIDIUM 70

1 25342U 98032A 04313.04333889 .00000021 00000-0 51162-6 0 4839
2 25342 86.3979 348.1403 0002370 86.7553 273.3915 14.34216863339181

IRIDIUM 72

1 25343U 98032B 04313.51903535 -.00000170 00000-0 -67684-4 0 4520
2 25343 86.3974 347.8420 0002378 86.4439 273.7048 14.34216110339254

IRIDIUM 73

1 25344U 98032C 04313.48610514 .00000287 00000-0 73883-4 0 3400
2 25344 86.4425 343.7908 0001845 74.3151 285.8272 14.46717163341543

IRIDIUM 74

1 25345U 98032D 04313.51269094 .00000066 00000-0 16608-4 0 4686
2 25345 86.3974 347.8997 0002411 84.6886 275.4588 14.34217431339254

IRIDIUM 75

1 25346U 98032E 04313.45560786 .00000120 00000-0 35787-4 0 4738
2 25346 86.3978 347.9555 0002394 88.8951 271.2523 14.34217312339812

IRIDIUM 3

1 25431U 98048A 04313.23069558 .00000235 00000-0 76864-4 0 4476
2 25431 86.3999 19.6123 0002302 86.2562 273.8896 14.34220299325727

IRIDIUM 76

1 25432U 98048B 04313.24972310 -.00000099 00000-0 -42467-4 0 3827
2 25432 86.3994 19.5082 0002787 48.4417 311.6979 14.34217751325713

IRIDIUM 82

1 25467U 98051A 04313.42832339 .00000022 00000-0 69074-6 0 6153
2 25467 86.3957 145.8117 0001751 131.0513 229.0844 14.34216604326752

IRIDIUM 81

1 25468U 98051B 04313.42198101 .00000029 00000-0 34030-5 0 4244
2 25468 86.3961 145.8262 0002251 82.4207 277.7246 14.34216891322978

IRIDIUM 80

1 25469U 98051C 04313.47272231 .00000095 00000-0 26783-4 0 4188
2 25469 86.3951 145.8238 0002295 76.5728 283.5738 14.34217000322986

IRIDIUM 77

1 25471U 98051E 04313.41971241 .00000016 00000-0 -13059-5 0 5944
2 25471 86.5148 145.8470 0002309 80.5320 279.6150 14.54938697327596

IRIDIUM 2

1 25527U 98066A 04313.26514498 .00002006 00000-0 17672-3 0 6014
2 25527 85.5631 156.9203 0012877 73.4445 286.8197 14.95830137326574

IRIDIUM 86

1 25528U 98066B 04313.49113828 .00000089 00000-0 15640-4 0 5777
2 25528 86.5099 114.0987 0002279 77.9338 282.2149 14.54938693319179

IRIDIUM 84

1 25530U 98066D 04313.53906665 .00000221 00000-0 71952-4 0 2935
2 25530 86.3909 114.2007 0002241 82.7763 277.3709 14.34217306317152

IRIDIUM 83

1 25531U 98066E 04313.50101313 .00000157 00000-0 48868-4 0 3894
2 25531 86.3907 114.1723 0002205 80.4883 279.6596 14.34217169314505

IRIDIUM 11

1 25577U 98074A 04313.28143944 -.00000033 00000-0 -18731-4 0 3839
2 25577 86.3993 19.4859 0002321 84.5421 275.6030 14.34216541308559

IRIDIUM 20

1 25578U 98074B 04313.26043593 -.00000684 00000-0 -16422-3 0 4968
2 25578 86.5179 19.5469 0002318 83.0958 277.0518 14.54935802312991

IRIDIUM 14

1 25777U 99032A 04313.18796013 .00000370 00000-0 81117-4 0 4376
2 25777 86.5166 348.0140 0002519 86.5474 273.6014 14.54940391287362

IRIDIUM 21

1 25778U 99032B 04313.19428004 .00000359 00000-0 78599-4 0 4085
2 25778 86.5162 347.9782 0002472 86.8717 273.2763 14.54941013287336

IRIDIUM 90

1 27372U 02005A 04313.50386039 .00000717 00000-0 12487-3 0 9308
2 27372 86.5814 51.1851 0009074 56.2884 303.9213 14.66608556146682

IRIDIUM 91

1 27373U 02005B 04313.49787875 .00000797 00000-0 13948-3 0 9356
2 27373 86.5811 51.1040 0002442 80.4429 279.7071 14.66612506146688

IRIDIUM 94

1 27374U 02005C 04313.51022623 .00000766 00000-0 13383-3 0 9341
2 27374 86.5812 51.0229 0002214 87.0499 273.0980 14.66609264146688

IRIDIUM 95

1 27375U 02005D 04313.37991549 .00000679 00000-0 11824-3 0 9327
2 27375 86.5808 51.1436 0002619 79.1880 280.9676 14.66608378146662

IRIDIUM 96

1 27376U 02005E 04313.52254565 -.00000354 00000-0 -68040-4 0 9319
2 27376 86.5801 51.0054 0002434 76.3374 283.8075 14.66604855146686

IRIDIUM 97

1 27450U 02031A 04313.52619366 .00000637 00000-0 11066-3 0 8355
2 27450 86.5765 82.7358 0002131 84.4951 275.6512 14.66608687127828

IRIDIUM 98

1 27451U 02031B 04313.52000857 .00000280 00000-0 46305-4 0 8275
2 27451 86.5760 82.7149 0002188 84.0475 276.1039 14.66604273127828

Bibliography

1. The Commission to Assess United States National Security Space Management and Organization, Report of the Commission to Assess United States National Security Space Management and Organization - Executive Summary, section 1623 of the National Defense Authorization Act for Fiscal Year 2000 (Public Law 106-65) , 11 Jan 2001
2. <http://www.af.mil>, accessed 23 Feb 05
3. Joint Doctrine for Space Operations, JP3-14. 9 Aug 2002
4. Dereniak, Eustace L. and Boreman, G., “Infrared Detectors and Systems”, Wiley-Interscience, 1996, p.66
5. Ibid
6. Ibid, p. 68
7. Ibid, p. 77
8. Ibid, p. 25
9. “Diffraction-Limited Imaging Using Large Ground-Based Visible and IR Telescopes”, <http://www.srl.caltech.edu/compastro/bispectrum.html>, accessed 4 Feb 05
10. Henderson, Tom, “The Physics Classroom”, <http://www.glenbrook.k12.il.us/gbssci/phys/Class/refln/u1311d.html>
11. Dereniak, Eustace L. and Boreman, G., *Infrared Detectors and Systems*, Wiley-Interscience, 1996, p. 212
12. Westlund, Harold B. and Gary W. Meyer, “A BRDF Database Employing the Beard-Maxwell Reflection Model”, Department of Computer and Information Science, University of Oregon
13. Ibid.
14. Moidel, C., “Bi-Directional Reflectance Distribution Functions”, http://www.cs.wpi.edu/~emmanuel/courses/cs563/write_ups/chuckm/chuckm_BRD Fs_overview.html accessed 26 Oct 04

-
15. Mungan, C., “Bidirectional Reflectance Distribution Functions, Describing First-Surface Scattering”, Summer 1998
 16. Ibid.
 17. Constantino, Joe, Air Force Research Lab, Optical Measurement Facility, email correspondence, 28 Oct 04
 18. Deak, Daniel, <http://www.obsat.com/images/iridium/flare.jpg>, accessed 27 Feb 05
 19. Constantino, Joe, Air Force Research Lab, Optical Measurement Facility, email correspondence, 28 Oct 04
 20. Schowengerdt, Robert A., Lecture Notes, “Optical Remote Sensing”, University of Arizona, 2003
 21. SaVi satellite constellation visualizer, <http://sourceforge.net/projects/savi/> accessed 22 Oct 04
 22. Iridium, LLC.
 23. Dorreman, Chris, <http://www.satobs.org/iridium.html> accessed 22 Oct 04
 24. Fleming, John, <http://satobs.org/seesat/Jan-1998/0326.html>
 25. ----. “The Iridium Satellite Constellation”, <http://satobs.org/iridium.html#iridium>
 26. Newsam, Andrew, Lecture Notes, Astronomy Fundamentals, Liverpool John Moores University, 2004
 27. “SPOT 4 Thermal Control”, http://spot4.cnes.fr/spot4_gb/thermic.htm accessed 31 Jan 05
 28. Hafemeister, David A., “Infrared Monitoring of Nuclear Power in Space”, Science & Global Security, 1989, Volume 1, pp.109-128
 29. Aftergood, Steven, “Background on nuclear Power in Space”, Science & Global Security, 1989, Volume 1, pp.93-107
 30. Ibid.
 31. Matson, Rob, IridFlar v2.21, <http://satobs.org/seesat/Mar-2002/0047.html>, 4 Mar 02

-
32. Maley, Paul, <http://www.meteorobs.org/maillist/msg07021.html>, accessed 27 Feb 05
 33. Ibid.
 34. Kelso, T., <http://celestrak.com/NORAD/elements/>, accessed 1 Jun 04
 35. Kelso, T., <http://celestrak.com/NORAD/elements/Section913.pdf>, accessed 27 Feb 05
 36. Constantino, Joe, Air Force Research Lab, Optical Measurement Facility
 37. Hafemeister, David A., “Infrared Monitoring of Nuclear Power in Space”, *Science & Global Security*, 1989, Volume 1, pp.109-128
 38. Kidger, Mark, <http://www.iac.es/proyect/CCam/Atmosphere.htm>, accessed 7 Mar 05
 39. Kelso, T., <http://celestrak.com/NORAD/elements/>, accessed 1 Jun 04

Vita

As an Airman, Capt Funge was a Biomedical Equipment Technician, assigned to Wilford Hall, the largest hospital in the United States Air Force. Within one year of his assignment to Lackland AFB, he was selected for Officer Training School (OTS).

After graduating OTS, and subsequent space operations training courses, he was assigned to the 3rd Space Operations Squadron at then Falcon AFB (Schriever AFB), Colorado. There he was a Satellite Vehicle Operator, instructor and satellite engineer for the Defense Satellite Communications System, Phase III (DSCS III) constellation. His tour at 3 SOPS cumulated with the successful launch of two DSCS III satellites and the safe disposal of the oldest bird in the fleet. While there he also earned a Masters of Engineering in Space Operations from the University of Colorado, Colorado Springs.

Capt Funge's next assignment was to the 4th Space Surveillance Squadron (subsequently realigned to the 4th Space Control Squadron) at Holloman AFB, New Mexico. There, he trained as a Crew Commander on the Deployable Space Support Segment, Phase I. His system expertise was noticed when he was hand-picked to lead a team augmenting the 76th Space Control Squadron when it deployed in support of Operations Enduring Freedom and Iraqi Freedom.

While deployed Capt Funge was selected as a Vigilant Scholar to attend the Air Force Institute of Technology. Shortly after reporting from overseas, he transferred to AFIT at Wright-Patterson AFB, Ohio. His studies will led to the award of a Masters of Science in Applied Physics. His next assignment was back in New Mexico at the Air Force Safety Center, Kirtland AFB.

REPORT DOCUMENTATION PAGE				<i>Form Approved</i> OMB No. 074-0188	
<p>The public reporting burden for this collection of information is estimated to average 1 hour per response, including the time for reviewing instructions, searching existing data sources, gathering and maintaining the data needed, and completing and reviewing the collection of information. Send comments regarding this burden estimate or any other aspect of the collection of information, including suggestions for reducing this burden to Department of Defense, Washington Headquarters Services, Directorate for Information Operations and Reports (0704-0188), 1215 Jefferson Davis Highway, Suite 1204, Arlington, VA 22202-4302. Respondents should be aware that notwithstanding any other provision of law, no person shall be subject to a penalty for failing to comply with a collection of information if it does not display a currently valid OMB control number.</p> <p>PLEASE DO NOT RETURN YOUR FORM TO THE ABOVE ADDRESS.</p>					
1. REPORT DATE (DD-MM-YYYY)		2. REPORT TYPE Master's Thesis		3. DATES COVERED (From – To) Sep 2003 – Mar 2005	
4. TITLE AND SUBTITLE DAYTIME DETECTION OF SPACE OBJECTS				5a. CONTRACT NUMBER	
				5b. GRANT NUMBER	
				5c. PROGRAM ELEMENT NUMBER	
6. AUTHOR(S) Funge, Alistair D., Captain, USAF				5d. PROJECT NUMBER	
				5e. TASK NUMBER	
				5f. WORK UNIT NUMBER	
7. PERFORMING ORGANIZATION NAMES(S) AND ADDRESS(S) Air Force Institute of Technology Graduate School of Engineering and Management (AFIT/EN) 2950 Hobson Way, Building 640 WPAFB OH 45433-8865				8. PERFORMING ORGANIZATION REPORT NUMBER AFIT/GAP/ENG/05-01	
9. SPONSORING/MONITORING AGENCY NAME(S) AND ADDRESS(ES)				10. SPONSOR/MONITOR'S ACRONYM(S)	
				11. SPONSOR/MONITOR'S REPORT NUMBER(S)	
12. DISTRIBUTION/AVAILABILITY STATEMENT APPROVED FOR PUBLIC RELEASE; DISTRIBUTION UNLIMITED.					
13. SUPPLEMENTARY NOTES					
14. ABSTRACT <p>Space Situational Awareness (SSA) requires repeated object updates for orbit accuracy. Detection of unknown objects is critical. A daytime model was developed that evaluated sun flares and assessed thermal emissions from space objects.</p> <p>Iridium satellites generate predictable sun glints. These were used as a model baseline for daytime detections. Flares and space object thermal emissions were examined for daytime detection. A variety of geometric, material and atmospheric characteristics affected this daytime detection capability.</p> <p>In a photon noise limited mode, simulated Iridium flares were detected. The peak Signal-to-Noise Ratios (SNR) were 6.05e18, 9.63e5, and 1.65e7 for the nighttime, daytime and infrared flares respectively.</p> <p>The thermal emission of space objects at 353K, 900K and 1300K with 2 to 20 m2 emitting areas were evaluated. The peak emission was for the 20 m2 900K object with an SNR of 1.08e10.</p> <p>A number of barriers remain to be overcome if daytime detection of space objects can be achieved. While the above SNR values are large, this is based on optimal detection. The SBR's were less than 1 for all cases. Image post-processing will be necessary to extract the object from the background.</p> <p>Successful daytime detection techniques will increase sensor utilization times and improve SSA.</p>					
15. SUBJECT TERMS					
16. SECURITY CLASSIFICATION OF:			17. LIMITATION OF ABSTRACT	18. NUMBER OF PAGES	19a. NAME OF RESPONSIBLE PERSON
a. REPORT	b. ABSTRACT	c. THIS PAGE			19b. TELEPHONE NUMBER (Include area code)
U	U	U	U	106	Matt Goda, Maj, USAF (937) 255-3636, ext 3614 matthew.goda@afit.edu

